

# A Kinetic Route to Helicity-Constrained Decay

Dion Li\*

Plasma Science and Fusion Center, Massachusetts Institute of Technology, Cambridge, MA 02139, USA

(Dated: February 20, 2026)

Through 2D3V PIC simulations of freely decaying sub-ion turbulence, intermittent localized regions with  $\mathbf{E} \cdot \mathbf{B} \neq 0$  are found to be statistically associated with reductions in the magnitude of magnetic helicity while evolving in the early electron-scale interaction phase. Motivated by this behavior, we propose a source-compensated, history-dependent helicity density that satisfies an exact local balance identity by construction, enabling Saffman-type two-point correlation integrals which, under standard flux-decorrelation assumptions, can exhibit intermediate-scale plateaus that are roughly time-independent. In our simulations we demonstrate such plateaus to remain approximately invariant even as the usual Saffman helicity integral plateau value  $I_H$  evolves during the early kinetic stage. Under approximate single-scale self-similarity, the plateau behavior of the magnetic integral is consistent with the 2D decay constraint  $BL \sim \text{const}$ . For initially net-helical configurations, we observe rapid development of mixed-signed magnetic helicity patches and a decrease of the global fractional helicity, such that the decay over the kinetic interval is again most consistent with the cancellation-dominated scaling constraint.

## I. INTRODUCTION

In ideal magnetohydrodynamics (MHD), the total magnetic helicity  $H_V = \int_V dV h$ , with  $h = \mathbf{A} \cdot \mathbf{B}$  the magnetic helicity density, is gauge-invariant and conserved in a simply connected domain when  $\partial V$  is a magnetic, impermeable boundary, or otherwise arranged so boundary terms vanish [1–5]. As a global topological measure of field-line twist, writhe, and linkage [6, 7],  $H_V$  plays a central organizing role in magnetic relaxation and turbulent decay. In high-Lundquist-number plasmas, magnetic helicity often remains comparatively well conserved, provided boundary fluxes are weak [8–11]. Because resistive dissipation is gradient-weighted and thus acts most strongly at small scales [12], and because helical turbulence tends to transfer magnetic helicity to larger scales [13–18], the total magnetic helicity usually decays more slowly than magnetic energy at high Lundquist numbers, making it a natural approximate invariant that constrains the late-time decay of magnetic turbulence [19–23].

For fully helical fields dominated by a single energy-containing scale,  $L$  (see, e.g., Eq. 55), conservation of magnetic helicity implies  $B^2 L \sim \text{const}$  [16, 24, 25], with the  $B$  (or  $B_{\text{rms}}$ ) the rms magnetic field. A distinct but common situation arises when the configuration is globally nonhelical in the sense that net magnetic helicity cancels, even though strong local magnetic helicity fluctuations persist. For such configurations, Hosking and Schekochihin [26] proposed a Saffman-type integral built from two-point correlations of magnetic helicity density,

$$\mathcal{I}_H(R) \equiv \int_{V_R} d^3r \langle h(\mathbf{x})h(\mathbf{x} + \mathbf{r}) \rangle, \quad (1)$$

with  $\langle \cdot \rangle$  an ensemble average. Under suitable scale separation,  $\mathcal{I}_H(R)$  can develop an intermediate-range plateau

that is approximately conserved. Indeed, Zhou *et al.* [27] confirmed that  $\mathcal{I}_H(R)$  approaches an  $R$ -independent asymptote  $I_H$  for  $L \ll R \ll L_{\text{sys}}$  [see also 28, 29], with  $L_{\text{sys}}$  the system domain size. Under the same scale-separation/localization assumptions, conservation of  $I_H$  yields  $B^4 L^5 \sim \text{const}$  in 3D [26, 30–32].

A key limitation of these helicity-based constraints is that many astrophysical and space plasmas do not remain in the ideal-MHD regime across all dynamically active scales [33–37]. Once the ideal-MHD ordering breaks down, magnetic helicity need not be conserved even in the absence of explicit resistive dissipation, because the magnetic helicity density obeys the general evolution law [3, 38]

$$\frac{\partial h}{\partial t} - c \nabla \cdot (\mathbf{A} \times \mathbf{E} - \varphi \mathbf{B}) = -2c \mathbf{E} \cdot \mathbf{B}, \quad (2)$$

with  $\varphi$  the electric potential. The source term  $-2c \mathbf{E} \cdot \mathbf{B}$  implies that any localized nonideal region with  $\mathbf{E} \cdot \mathbf{B} \neq 0$  permits magnetic helicity change [39]. This mechanism is particularly relevant at sub-ion scales, where electrons can be strongly non-frozen-in within electron diffusion regions (EDRs) [33, 40] and  $\mathbf{E} \cdot \mathbf{B}$  is not controlled by a small resistivity, becoming dynamically significant [41–47].

Such localized nonideal regions arise naturally in kinetic turbulence. A broad body of kinetic [48–51] and hybrid-kinetic [52–56] work, together with in-situ space-plasma evidence [57–62], has shown in a wide variety of settings that turbulence rapidly generates intermittent current sheets at ion scales, many of these sheets reconnect, and reconnection commonly coincides with localized dissipation and heating signatures. In sufficiently thin current sheets, reconnection can occur in an “electron-only” mode [33, 40], with observational [63–65] and numerical [66–70] evidence for electron-only reconnection (EOR) having grown substantially over the last decade. Thus the classical magnetic helicity constraint that organizes MHD decay competes with localized ki-

\* dionli@psfc.mit.edu

netic nonideality at the very scales where turbulence becomes most intermittent. This competition motivates two closely related questions: i) How does collisionless, reconnection-mediated nonideality modify magnetic helicity at sub-ion scales? ii) If the traditional ideal MHD magnetic helicity constraint is compromised, is there a first-principles kinetic analogue that can still provide a practically useful decay constraint?

In this paper we provide possible answers to both questions in the specific setting of freely decaying 2D3V turbulence at sub-ion scales. In Section II, using magnetic helicity balance and reconnection energetics, we find evidence that during the early kinetic phase the intermittent  $\mathbf{E} \cdot \mathbf{B} \neq 0$  term is statistically associated with structure-handedness proxies and is often accompanied by a reduction in the magnitude of magnetic helicity contained within individual coherent structures. In Section III, we develop a fully kinetic reformulation that can be used to motivate decay constraints. Starting from the Vlasov-Maxwell system and taking velocity moments without closure, we write the canonical vorticity transport [71–75] for each species and obtain a local continuity equation with a kinetic source term. We then absorb the time-integrated source into a reweighted, history-dependent density so that it obeys a source-free conservation identity by construction. While this step is explicitly an accounting reformulation rather than a new topological invariant, it motivates kinetic Saffman-type two-point integrals which—under standard flux-decorrelation assumptions [e.g., 26, 29]—can admit intermediate-scale plateaus that are operationally identifiable and can be tested directly in simulations.

We focus primarily on the magnetic component of the conserved density because it reduces to the usual magnetic helicity density in the ideal MHD limit and is most directly relevant when flows are initially absent or subdominant. In our 2D3V particle-in-cell (PIC) simulations, the associated two-point integral exhibits a roughly time-independent plateau over a measurable range of window sizes while the usual helicity-based Hosking/Saffman integral plateau value  $I_H$  evolves during the kinetic stage.  $I_H$  only recovers approximate invariance when  $\mathbf{E} \cdot \mathbf{B}$  becomes statistically uncorrelated with structure-handedness proxies and/or once  $\mathbf{E} \cdot \mathbf{B}$  becomes comparatively small as the dominant scales move above electron kinetic scales. Under approximate single-scale self-similarity, the plateau behavior is consistent with a simple decay scaling, i.e.,  $BL \sim \text{const}$  in 2D3V, and we present numerical evidence compatible with this scaling.

Finally in Section IV, we address a contrasting case with initially net-helical fields, where we observe that turbulent reconnection quickly develops mixed-signed magnetic helicity patches. As a result, the kinetic-scale dynamics tend toward an effectively nonhelical state and the measured decay is again most consistent with  $BL \sim \text{const}$ .

To test these ideas across both cancellation-dominated

and net-helical initial conditions, we adopt the global fractional magnetic helicity

$$\sigma = \frac{\int_0^\infty dk \sigma_k(k) \mathcal{E}_B(k)}{\int_0^\infty dk \mathcal{E}_B(k)} \in [-1, 1], \quad (3)$$

with  $\sigma_k(k) \equiv k H_k(k) / \mathcal{E}_B(k) \in [-1, 1]$  the fractional magnetic helicity spectrum [e.g., 76–78] and  $\mathcal{E}_B(k)$  and  $H_k(k)$  the magnetic energy and helicity spectra, respectively. For our numerical simulations, we focus on  $\sigma_0 \equiv \sigma(t=0) = \{0, 1\}$ . Because fully kinetic turbulence spans disparate ion and electron scales, we perform 2D3V PIC runs at both reduced,  $m_i/m_e = 25$ , and realistic,  $m_i/m_e \approx 1836$ , mass ratios. The reduced-ratio runs make it feasible to reach adequate resolution, statistics, and dynamical range in a finite domain, while the realistic-ratio runs verify that the key behaviors reported here persist when the physical ion-electron scale separation is correctly represented and also help identify which quantitative differences are genuinely controlled by that separation.

## II. MAGNETIC HELICITY EVOLUTION AT SUB-ION SCALES

To assess the implications of sub-ion nonideality on magnetic helicity, we analyze our freely decaying 2D3V PIC simulations (see Appendix A for the setup and details of our numerical experiments) with  $\partial_z = 0$ ; the correlations reported below should therefore be interpreted as tendencies within this geometry and initial-condition class. In this geometry it is convenient to write [79]

$$\mathbf{B} = \nabla A_z \times \hat{\mathbf{z}} + \hat{\mathbf{z}} B_z, \quad (4)$$

with  $A_z(x, y)$  the out-of-plane component of the magnetic vector potential. Equation 4 implies  $\mathbf{B} \cdot \nabla A_z = 0$ , so the level sets  $A_z = \text{const}$  are magnetic surfaces. This makes  $A_z$ -contour-bounded structures a natural diagnostic object in 2D3V. Hence we define the boundary of an individual coherent structure  $s$  at each time by a closed  $A_z$  contour and consider the fixed-gauge diagnostic [80]

$$H_{V_s} = \int_{V_s} dV \mathbf{A} \cdot \mathbf{B}. \quad (5)$$

Because  $V_s$  is defined by an instantaneous  $A_z$  contour, it is time-dependent and  $dH_{V_s}/dt$  contains, in general (see, e.g., Eq. 2), (i) the nonideal volume contribution  $-2c \int_{V_s} dV \mathbf{E} \cdot \mathbf{B}$  and (ii) transport/exchange contributions across the moving structure boundary. The  $A_z = \text{const}$  choice implies  $\mathbf{B} \cdot \hat{\mathbf{n}} = 0$  on the structure sidewall, which removes the  $\varphi \mathbf{B}$  contribution there, but it does not in general eliminate  $\mathbf{A} \times \mathbf{E}$  transport or the additional moving-boundary term associated with  $V_s = V_s(t)$ . In what follows, we use  $-2c \int_{V_s} dV \mathbf{E} \cdot \mathbf{B}$  as the primary source term for magnetic helicity change within interacting structures and interpret the remaining contributions

as magnetic helicity redistribution among neighboring regions.

In the context of collisionless reconnection, the generalized Ohm's law gives the nonideal electric field in the electron frame [33, 40, 45]

$$\mathbf{E}' = \mathbf{E} + \frac{\mathbf{u}_e \times \mathbf{B}}{c} = -\frac{1}{en} \nabla \cdot \mathbf{\Pi}_e - \frac{m_e}{e} [\partial_t \mathbf{u}_e + (\mathbf{u}_e \cdot \nabla) \mathbf{u}_e], \quad (6)$$

supported in the EDR by the divergence of the electron pressure tensor  $\mathbf{\Pi}_e$  and by electron inertia. Here,  $e > 0$  and  $\mathbf{u}_e$  is the electron flow. In our simulations, during the interactions of coherent structures at sub-ion scales and near  $d_e = (m_e c^2 / 4\pi n e^2)^{1/2}$ , the electron skin-depth or inertial length, regions identified operationally as EDR-like exhibit a statistical association between the sign of  $\mathbf{E} \cdot \mathbf{B}$  and structure handedness as measured by a current helicity proxy [81–83], e.g.  $\mathbf{J} \cdot \mathbf{B}$  or [e.g., 2, 9, 84]

$$\alpha \equiv \mathbf{J} \cdot \mathbf{B} / |\mathbf{B}|^2, \quad (7)$$

with  $\mathbf{J}$  the current density from species flows. We decompose  $\mathbf{J}$  into components parallel and perpendicular to  $\hat{\mathbf{b}} \equiv \mathbf{B}/|\mathbf{B}|$ :

$$\mathbf{J} = (\mathbf{J} \cdot \hat{\mathbf{b}}) \hat{\mathbf{b}} + (\mathbb{I} - \hat{\mathbf{b}} \otimes \hat{\mathbf{b}}) \cdot \mathbf{J} = J_{\parallel} \hat{\mathbf{b}} + \mathbf{J}_{\perp}, \quad (8)$$

thus giving  $J_{\parallel} = \alpha |\mathbf{B}|$  and  $\alpha \mathbf{E} \cdot \mathbf{B} = E'_{\parallel} J_{\parallel}$ .

A widely used electron-frame energy conversion proxy for identifying and characterizing EDRs in collisionless reconnection is the quantity  $\mathbf{E}' \cdot \mathbf{J}$  [85–90], which can be decomposed into  $E'_{\parallel} J_{\parallel}$  and  $\mathbf{E}'_{\perp} \cdot \mathbf{J}_{\perp}$ . Which of these terms dominate depends strongly on reconnection geometry, especially the guide-field: antiparallel/low-guide cases tend to be perpendicular-dominated near the inner EDR [91–93], whereas guide-field reconnection can be parallel-dominated [94–97]. In our numerical simulations with  $\beta \equiv 8\pi(n_i T_i + n_e T_e)/B^2 \sim 1$ , we find empirically that

$$\mathbf{E} \cdot \mathbf{B} \sim \mathbf{E}' \cdot \mathbf{J} / \alpha \quad (9)$$

in EDR-like regions, consistent with cases where the parallel conversion term contributes substantially to  $\mathbf{E}' \cdot \mathbf{J}$ , and that the signs predominantly agree:

$$\text{sgn}(\mathbf{E} \cdot \mathbf{B}) \simeq \text{sgn}(\mathbf{E}' \cdot \mathbf{J} / \alpha), \quad (10)$$

with intermittent exceptions, shown in Fig. 1. This figure demonstrates that  $\langle \mathbf{E} \cdot \mathbf{B} / (\mathbf{E}' \cdot \mathbf{J} / \alpha) \rangle_{V_{\text{sys}}}$ , the domain average of  $\mathbf{E} \cdot \mathbf{B} / (\mathbf{E}' \cdot \mathbf{J} / \alpha)$ , remains order-unity and tends to be positive throughout all numerical experiments. Figure 1 also shows that even at times when the domain average is negative, Eq. 10 is satisfied for a majority of the domain by area.

We relate  $\mathbf{E}' \cdot \mathbf{J}$  with the rate-of-change of the magnetic energy density by noting that energy exchange between fields and particles is governed by Poynting's theorem [98]

$$\partial_t \left( \frac{E^2 + B^2}{8\pi} \right) + \frac{c}{4\pi} \nabla \cdot (\mathbf{E} \times \mathbf{B}) = -\mathbf{E} \cdot \mathbf{J}, \quad (11)$$

and in our simulations, we find  $E_{\text{rms}}^2 / B_{\text{rms}}^2 \leq 1$  at all times, as shown in Fig. 2, so the rms electric energy density never exceeds that of the magnetic energy density. Even when  $E_{\text{rms}}^2 / B_{\text{rms}}^2$  becomes roughly constant at later times and approaches  $\approx 1$  in the globally nonhelical simulations, retaining or omitting  $\partial_t(E^2/8\pi)$  changes the instantaneous field-energy term by at most an order-unity factor. The bound  $E^2/B^2 \lesssim 1$  is consistent with subluminal, magnetically dominated electromagnetic fluctuations [99–101].

Over a selected interaction area, we use  $-\int_{V_s} dV \mathbf{E} \cdot \mathbf{J}$  as the primary source term for electromagnetic energy change within interacting structures and, as with the transport/exchange contributions to  $H_{V_s}$ , we interpret the remaining contributions as field-energy redistribution among neighboring regions. Assuming negligible ion response near electron scales, e.g.,  $\mathbf{u}_e \simeq -\mathbf{J}/en$  [40, 64, 66], Eq. 11 implies

$$\langle \mathbf{E}' \cdot \mathbf{J} \rangle_{V_s} \sim -\langle \dot{E}_B \rangle_{V_s} > 0, \quad (12)$$

where  $\langle \cdot \rangle_{V_s}$  denotes a spatial average over  $V_s$ ,  $E_B \equiv B^2/8\pi$  is the magnetic energy density, and the inequality in Eq. 12 is a statement of decaying turbulence, i.e.,  $\dot{E}_B < 0$  (see, e.g., the  $B_{\text{rms}}^4$  curve in Fig. 5).

From Eqs. 9, 10, and 12, we find that the structure-averaged nonideality satisfies the order-of-magnitude tendency

$$\langle \mathbf{E} \cdot \mathbf{B} \rangle_{V_s} \sim -\alpha_s^{-1} \langle \dot{E}_B \rangle_{V_s}, \quad (13)$$

provided that  $\alpha$  is approximately sign-coherent within the selected  $A_z$ -bounded structures. Here,

$$\alpha_s \equiv H_{C_s} \left( \int_{V_s} dV B^2 \right)^{-1}, \quad (14)$$

where

$$H_{C_s} = \int_{V_s} dV \mathbf{J} \cdot \mathbf{B} \quad (15)$$

is the current helicity in  $V_s$ . To quantify the handedness of each magnetic structure in a way that is directly comparable to  $\alpha_s$ , we compute for every  $A_z$ -bounded structure the structure-integrated proxies  $H_{V_s}$  and  $H_{C_s}$  and define a sign-alignment diagnostic

$$S \equiv \text{sgn}(H_{V_s}) \text{sgn}(H_{C_s}) \in \{\pm 1\}. \quad (16)$$

Our structure-by-structure measurements show that, at early times when sub-ion nonideality is strongest, a large majority of  $A_z$ -bounded structures exhibit the same handedness in magnetic and current helicity proxies, i.e.,

$$\text{sgn}(H_{V_s}) \simeq \text{sgn}(H_{C_s}), \quad (17)$$

as reported by Figs. 3, plotting the evolution of  $f_{S+}$ , the fraction of structures bounded by  $A_z$  contours for which  $S = +1$ , and 4, showing colormap representations of the

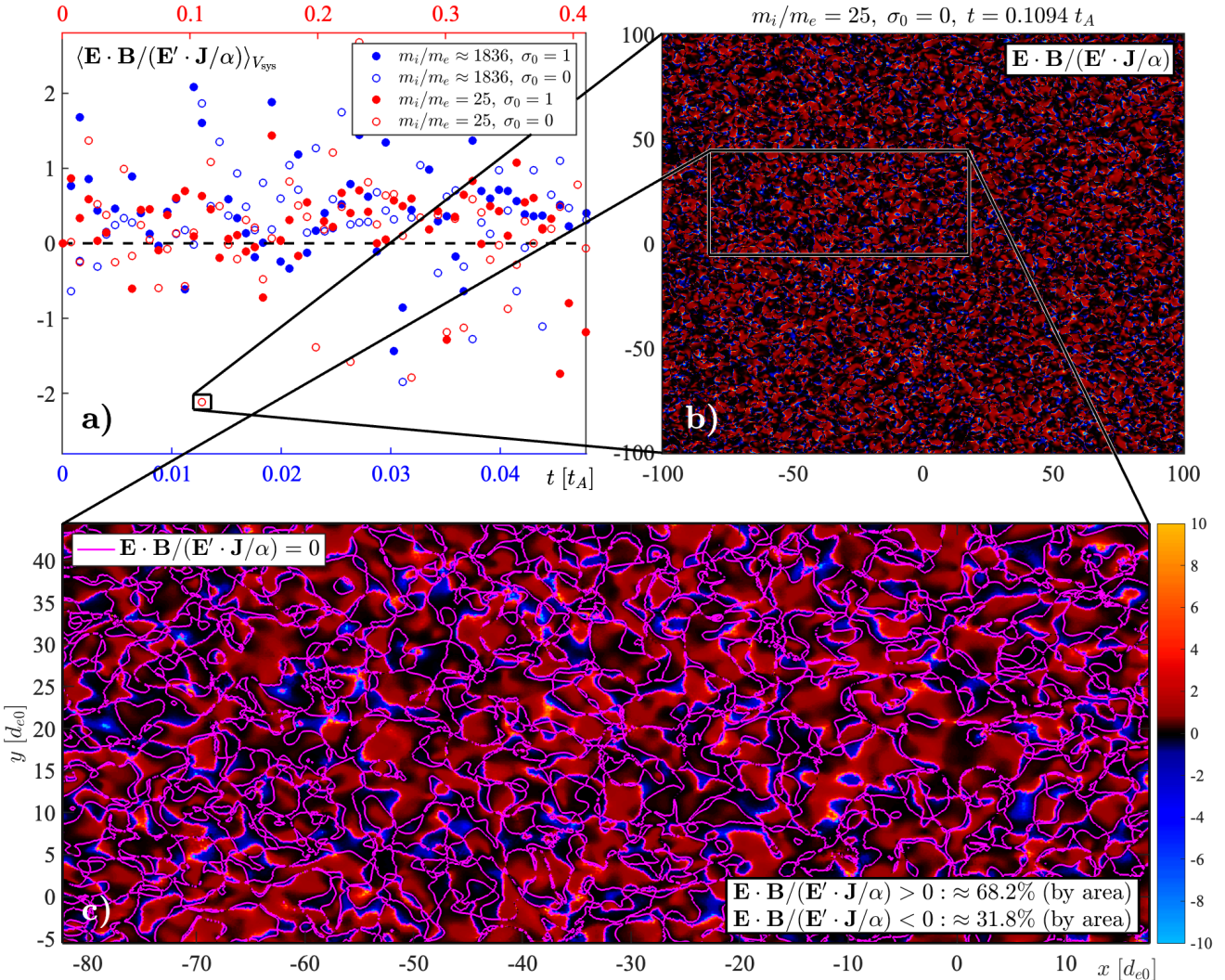


FIG. 1. Numerical evidence of Eqs. 9 and 10 for all simulations presented in this work (see Table I in Appendix A). (a) plots  $\langle \mathbf{E} \cdot \mathbf{B} / (\mathbf{E}' \cdot \mathbf{J} / \alpha) \rangle_{V_{\text{sys}}}$  at times spaced by  $\Delta t \approx [6.84 \times 10^{-3}, 7.98 \times 10^{-4}] t_A$  for  $m_i/m_e = 25$  and  $\approx 1836$ , respectively. Here,  $\langle \cdot \rangle_{V_{\text{sys}}}$  denotes an average over the entire spatial domain  $V_{\text{sys}}$ , and included as the black dashed line is when  $\langle \mathbf{E} \cdot \mathbf{B} / (\mathbf{E}' \cdot \mathbf{J} / \alpha) \rangle_{V_{\text{sys}}} = 0$ . (b) shows  $\mathbf{E} \cdot \mathbf{B} / (\mathbf{E}' \cdot \mathbf{J} / \alpha)$  over the entire domain for the strongest outlier shown in (a) ( $m_i/m_e = 25, \sigma_0 = 0$ , at time  $t = 0.1094 t_A$ ). (c) zooms in on (b) over an  $\approx [100 \times 50] d_{e0}$  subdomain (with  $d_{e0} = d_e(n_0) = (m_e c^2 / 4\pi n_0 e^2)^{1/2}$  and  $n_0$  the initial, uniform ion and electron number density) that consisted of the largest negative  $\mathbf{E} \cdot \mathbf{B} / (\mathbf{E}' \cdot \mathbf{J} / \alpha)$  average value. Included in (c) are contours where  $\mathbf{E} \cdot \mathbf{B} / (\mathbf{E}' \cdot \mathbf{J} / \alpha) = 0$  (in magenta). We find that even in this situation in which Eq. 10 appears to be contradicted most significantly, the majority of the subdomain consists of patches in which Eq. 10 is valid. For example,  $\mathbf{E} \cdot \mathbf{B}$  and  $\mathbf{E}' \cdot \mathbf{J} / \alpha$  share the same sign over nearly 70% of the box, whereas they differ in sign over approximately 30% of the subdomain.

structure-by-structure helicity sign alignment. At later times, occurring earlier for initially nonhelical configurations, the alignment becomes mixed, indicating that the ensemble no longer maintains a strong one-to-one sign correspondence between  $\mathbf{A} \cdot \mathbf{B}$  and  $\mathbf{J} \cdot \mathbf{B}$  at the structure level.

A natural interpretation of the observed early-time structure-level sign alignment is that in Fourier space the Ampère current helicity spectrum  $H_{CA,k}(k)$  is  $k^2$ -weighted magnetic helicity under isotropic condi-

tions [102], where the Ampère current is  $\mathbf{J}_A \equiv (c/4\pi)\nabla \times \mathbf{B}$  and the Ampère current helicity in  $V_s$  is defined as

$$H_{CA_s} = \int_{V_s} dV \mathbf{J}_A \cdot \mathbf{B}. \quad (18)$$

In other words,

$$H_{CA,k}(k) \simeq (c/4\pi)k^2 H_k(k) \quad (19)$$

in Coulomb-gauge if  $H_k$  is single-signed over the excited band within a coherent structure. In this situation,

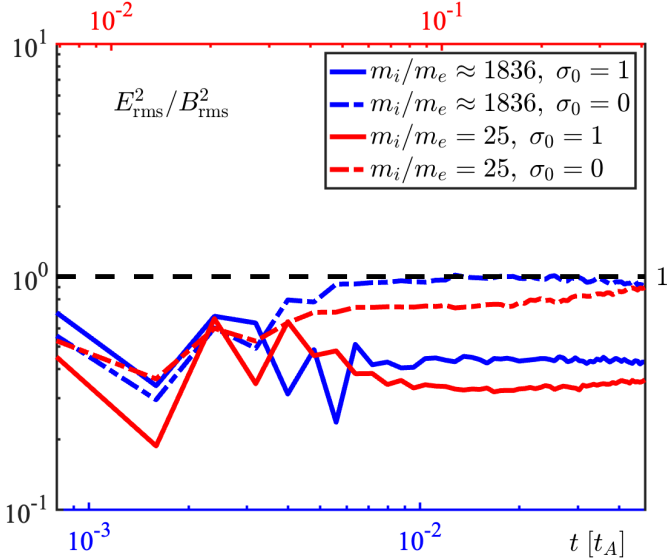


FIG. 2. Evolution of  $E_{\text{rms}}^2/B_{\text{rms}}^2$  for all 2D3V simulations presented in this work. Included as the black dashed line is when  $E_{\text{rms}}^2/B_{\text{rms}}^2 = 1$ .

$H_{V_s}$  and  $H_{CAs}$  are expected to share the same sign and  $\mathbf{J}_A \cdot \mathbf{B}$  is correspondingly sign-coherent within the dominant structures. A key subtlety of this argument is that it is most directly applicable when  $\mathbf{J}$  is identified with the Ampère current  $\mathbf{J}_A$ , whereas in our diagnostic we use the physical current  $\mathbf{J} = \sum_i q_i n_i \mathbf{u}_i$  [103], with  $i = i, e$  the particle species index. In collisionless sub-ion turbulence these currents need not coincide locally because the generalized Ohm's law (e.g., Eq. 6) permits substantial non-MHD contributions that can produce components of  $\mathbf{J}$  not simply tied to  $\nabla \times \mathbf{B}$ . Consequently, our early-time observation that  $\text{sgn}(H_{V_s}) \simeq \text{sgn}(H_{C_s})$  might indicate that the field-aligned, reconnection-relevant portion of the physical current remains largely organized by the structures' handedness during the strongly nonideal phase, while the later-time alignment-mixing plausibly reflects the growing importance of currents that contaminate  $\mathbf{J} \cdot \mathbf{B}$  relative to the Ampère current expectation.

Combining Eqs. 2, 13, and 17, we arrive at

$$|H_{V_s}|^{-1} \frac{d}{dt} \left( \frac{1}{2} H_{V_s}^2 \right) \sim 8\pi L \int_{V_s} dV \dot{E}_B < 0 \quad (20)$$

during the early kinetic phase, since

$$|\alpha|^{-1} \sim (4\pi/c) |\mathbf{B} \cdot (\nabla \times \mathbf{B})|^{-1} |\mathbf{B}|^2 \sim 4\pi L/c. \quad (21)$$

We interpret Eq. 20 as indicative that magnetic helicity depletion is not merely a consequence of global cancellation, but a dynamically preferred outcome correlated with magnetic energy conversion within the interaction area. In this sense, early-time reconnection at sub-ion scales acts as a mechanism that reduces the helical content of coherent structures while magnetic energy is simultaneously redistributed and dissipated. Because

structure boundaries are time-dependent, magnetic helicity can also be exchanged between neighboring regions by transport; nevertheless, Eq. 20 suggests that, during the dominant interaction intervals, the net effect of nonideality is to bias the evolution toward  $|H_{V_s}|$  depletion.

If correlated nonideality systematically reduces  $|h|$  within interacting structures, it will tend to reduce magnetic helicity variance  $\langle h^2 \rangle$  and hence  $I_H$  (see, e.g., Eq. 1). Consistent with this, the interval over which  $I_H$  decreases most rapidly coincides with the regime of high structure-level sign alignment, i.e., predominantly  $\text{sgn}(H_{V_s}) = \text{sgn}(H_{C_s})$ , whereas  $I_H$  becomes approximately stationary once the alignment becomes mixed at later times (see, e.g., Fig. 5) [104], consistent with our focus here on early-time magnetic helicity depletion driven by strong sub-ion nonideality.

Following the derivation in Appendix B, which determines for our configuration the numerical values of  $I_{\mathcal{L},1}$  (to be defined in Section III) and the initial  $I_H$ , for statistically homogeneous and isotropic fields, we may write the Hosking integral plateau value approximately as

$$I_H \simeq \frac{1}{16} \frac{S_{d-1}}{(2\pi)^d} \int_0^\infty dk [1 - \sigma_k^2(k)] k^{d-3} F^2(k). \quad (22)$$

Here,  $d$  is the number of spatial dimensions in the system under consideration, e.g.,  $d = 2$  for 2D3V,  $S_{d-1} = 2\pi^{d/2}/\Gamma(d/2)$  is the surface area of a unit  $(d-1)$ -sphere,  $\Gamma(\cdot)$  is the gamma function, and  $F(k)$  sets the spectrum

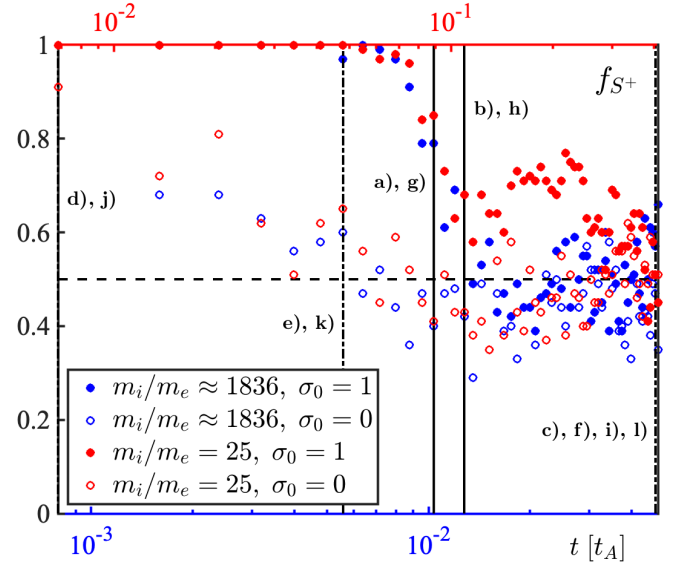


FIG. 3. Evolution of  $f_{S+}$ , the fraction of structures bounded by  $A_z$  contours for which  $S \equiv \text{sgn}(H_{V_s})\text{sgn}(H_{C_s}) = +1$ , for all 2D3V PIC simulations presented in this work. Indicated by the solid and dash-dotted black lines for initially net-helical and nonhelical configurations, respectively, are the times plotted in Fig. 4, with annotations indicating the corresponding subplot letter. The black dashed line indicates  $f_{S+} = 0.5$ .

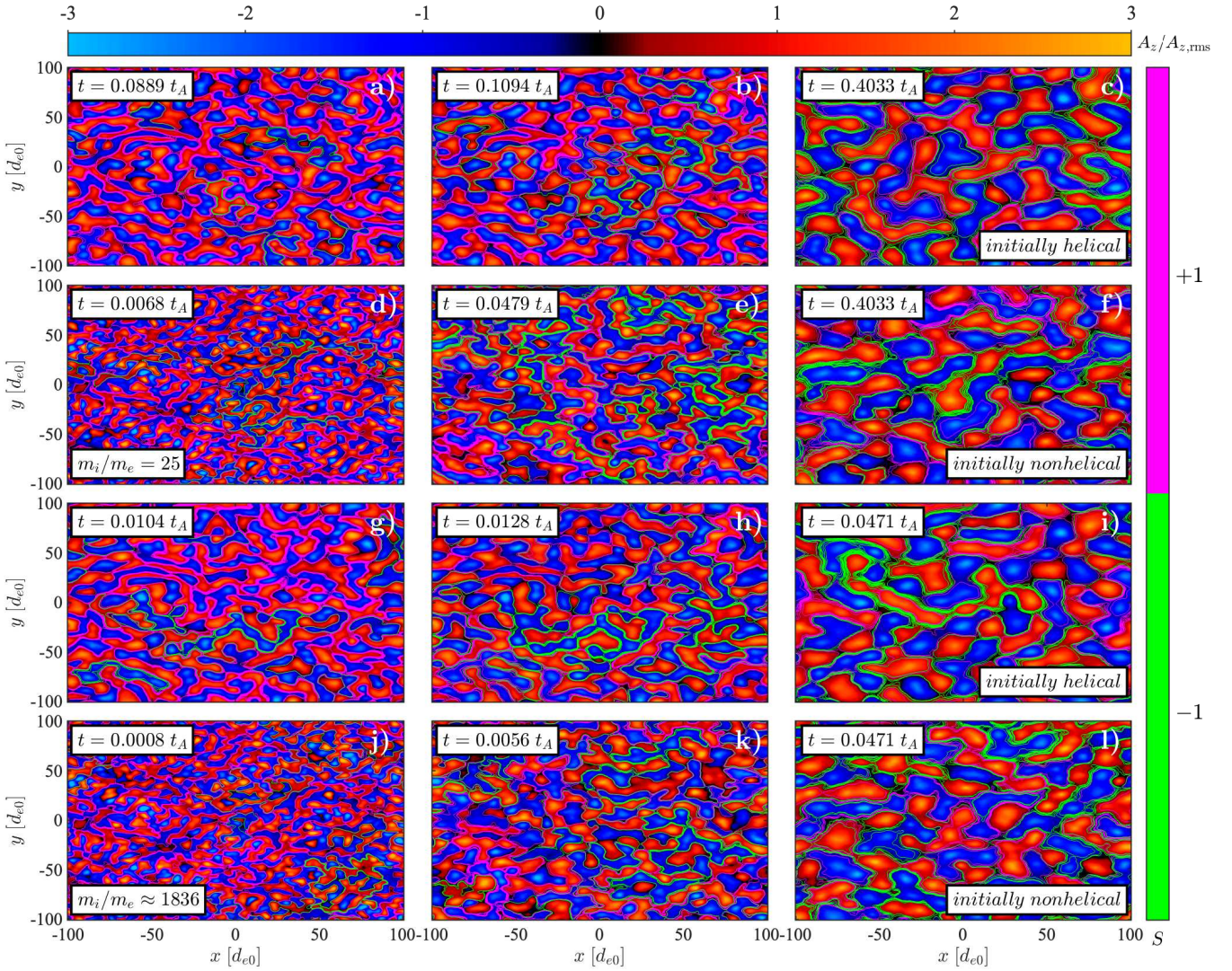


FIG. 4. Representation of the structure-by-structure helicity sign alignment in our 2D3V PIC simulations. Each panel shows the out-of-plane flux function  $A_z(x, y)$  (red-blue colormap) together with closed  $A_z = \text{const}$  contours (flux surfaces) that define individual coherent magnetic structures. For each structure  $s$ , we compute the structure-integrated helicity proxies  $H_{V_s} = \int_{V_s} dV \mathbf{A} \cdot \mathbf{B}$  (Eq. 5) and  $H_{C_s} = \int_{V_s} dV \mathbf{J} \cdot \mathbf{B}$  (Eq. 15), and color the structure boundary by the sign alignment  $S \equiv \text{sgn}(H_{V_s})\text{sgn}(H_{C_s}) \in \{\pm 1\}$  (Eq. 16; magenta denotes aligned signs,  $S = +1$ , and green denotes anti-aligned signs,  $S = -1$ ). Shown are three representative times (early (left column)/intermediate (middle column)/late (right column), indicated by the solid and dash-dotted black lines in Fig. 3) for each of the four simulations ( $m_i/m_e = 25$  (top rows) and  $\approx 1836$  (bottom rows) and  $\sigma_0 = 1$  (first and third rows) and 0 (second and fourth rows)). At early times—when sub-ion nonideality and reconnection-driven interactions are strongest—structure boundaries are predominantly magenta, indicating that a large majority of coherent structures satisfy  $\text{sgn}(H_{V_s}) \simeq \text{sgn}(H_{C_s})$ . At later times the population becomes mixed, showing comparable magenta/green, and in some cases majority green. This transition coincides with the regime in which  $I_H$  (see, e.g., Eq. 1) becomes approximately stationary (see, e.g., Fig. 5), whereas the early-time decline of  $I_H$  occurs during the high-alignment phase.

of the magnetic field via

$$B_{\text{rms}}^2 = \frac{1}{4} \frac{S_{d-1}}{(2\pi)^d} \int_0^\infty dk k^{d-1} F(k). \quad (23)$$

Equations 22 and 23 allow us to arrive at, with  $\sigma_k(k) \simeq \sigma = 0$ , i.e., globally nonhelical fields,

$$I_H B_{\text{rms}}^{-4} \propto L_h^{d+2}, \quad (24)$$

where we have denoted  $L_h$  as the “effective magnetic helicity density correlation length” [e.g., 27], defined via a spectral moment ratio

$$L_h \equiv \left\{ \frac{\int_0^\infty dk k^{d-3} F^2(k)}{[\int_0^\infty dk k^{d-1} F(k)]^2} \right\}^{1/(d+2)}, \quad (25)$$

intended to capture the scale dominating the magnetic helicity density two-point function  $\langle h(\mathbf{x})h(\mathbf{x}+\mathbf{r}) \rangle$ . We ar-

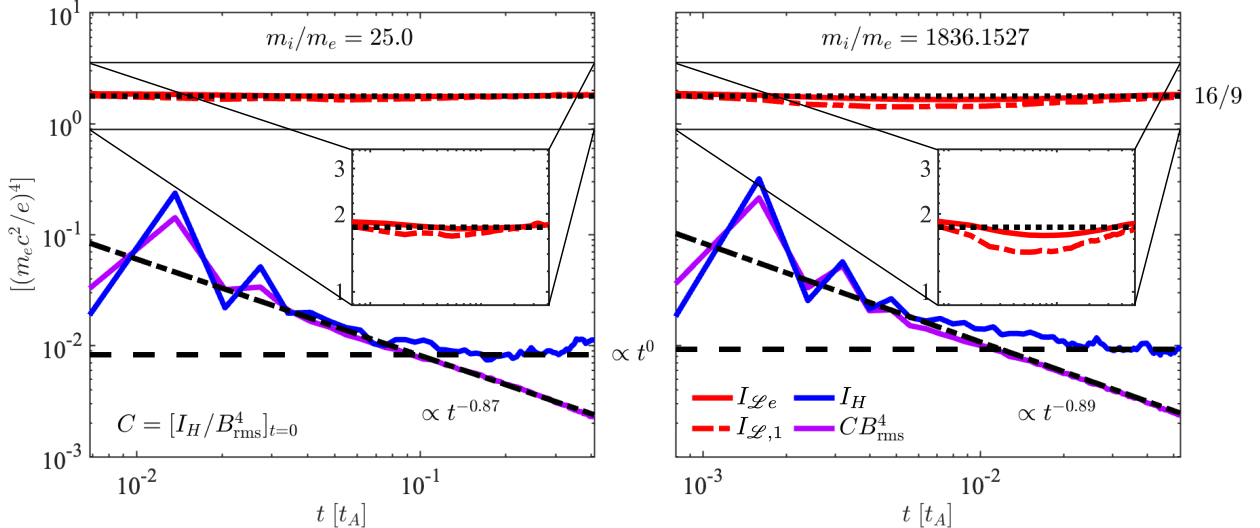


FIG. 5. Time evolution of  $I_{\mathcal{L}e}$  (solid red),  $I_{\mathcal{L},1}$  (dash-dotted red),  $I_H$  (solid blue), and  $B_{\text{rms}}^4$  (solid purple; multiplied by a proportionality constant equivalent to  $2\pi L_h^4(t=0)$ , indicated by the lower left annotation in the left panel) in globally nonhelical simulations with  $m_i/m_e = 25$  (left) and  $\approx 1836$  (right). Included (dotted black) is the calculated value of  $I_{\mathcal{L},1}(t=0) = I_H(t=0)$  ( $= I_{\mathcal{L}e}(t=0)$  for initially zero flow), derived in Appendix B. Also included are the power-law scalings:  $\propto t^{-0.87}$  for  $m_i/m_e = 25$  and  $\propto t^{-0.89}$  for  $m_i/m_e \approx 1836$  (dash-dotted black, fitted using the  $B_{\text{rms}}^4$  data) and  $\propto t^0$  (dashed black). The insets zoom in on the vertical axis range  $\in [1/2, 2] \times 16/9$ .

gue that because sub-ion nonideality impedes the transfer of helical content into larger structures via depletion, magnetic helicity density fluctuations may remain controlled by a kinetic correlation length  $L_h$  rather than by the growing outer-scale  $L$ . Indeed, we find for our globally nonhelical initial configurations that  $L_h \simeq \text{const}$  as indicated in Fig. 5, showing that  $I_H \propto B_{\text{rms}}^4$  at early times, consistent with the regime where  $H_{V_s}$  and  $H_{C_s}$  are sign-aligned. Also plotted in Fig. 5 are the numerical values of approximately conserved quantities  $I_{\mathcal{L}e}$  and  $I_{\mathcal{L},1}$  that we introduce in Section III.

Throughout this section we focused on the early, strongly nonideal phase of our 2D3V decaying turbulence simulations, during which intermittency and electron-scale reconnection signatures emerge rapidly from the initialized field. Because our initial magnetic field is constructed from a finite set of modes concentrated in a narrow band of wavenumbers (see Appendix A), the earliest structures inherit a comparatively narrow distribution of excited scales. The scalings and sign-correlations discussed in this section should therefore be interpreted as empirical tendencies within this class of initial conditions and geometry, and not as universal properties of all sub-ion turbulence regimes, e.g., broadband initial states, driven steady-state turbulence, or fully 3D systems, where boundary fluxes, scale bandwidth, and structure topology can materially alter magnetic helicity transport and proxy alignment [18, 105–109].

### III. SOURCE-COMPENSATED HELICITY

A central implication of Section II is that early-time sub-ion interactions are characterized by systematic magnetic helicity depletion, correlated with magnetic energy conversion. Equation 2 provides a natural bookkeeping identity for quantifying this depletion. Neglecting boundary fluxes over an interaction interval  $t \in [t_0, t_1]$ , the change in magnetic helicity is governed by the integrated nonideal source,

$$\Delta H_{V_s} = -2c \int_{t_0}^{t_1} dt' \int_{V_s} dV \mathbf{E} \cdot \mathbf{B}. \quad (26)$$

This motivates introducing the event-local quantity

$$\begin{aligned} \mathcal{L}_1(\mathbf{x}, t) \equiv h(\mathbf{x}, t) + 2c \\ \times \int_{t_0}^t dt' \mathbf{E}(\mathbf{x}, t') \cdot \mathbf{B}(\mathbf{x}, t'), \end{aligned} \quad (27)$$

which is constant in time in the absence of fluxes and, more generally, obeys a local conservation law when fluxes are retained (see, e.g., Eq. 39). For single-scale coherent structures,  $\mathcal{L}_1$  is useful as an organizing variable because both the instantaneous  $h$  and the time-integrated source term naturally have the same macroscopic dimensions as  $B^2 L$ . The empirical correlation expressed by Eq. 20 further suggests that the same interaction-scale length  $L$  controlling magnetic energy conversion also controls the accumulation of  $-2c \int_{t_0}^t dt' \mathbf{E} \cdot \mathbf{B}$  over the event,

making it plausible that  $\mathcal{L}_1$  provides a quasi-structural label whose amplitude is proportional, up to order-unity, event-dependent factors, to  $B^2L$ . In this section, we therefore treat

$$\mathcal{L}_1 \sim B^2L \quad (28)$$

as a working hypothesis—motivated by the observed early-time coupling between magnetic helicity depletion and energy conversion—and use it to motivate a Saffman-type correlation integral for deriving scaling constraints in globally nonhelical configurations. We discuss, at the end of this section, the validity of interpreting Eq. 28 as indicative that sub-ion interactions between like-helicity structures are  $B^2L$ -preserving processes.

To rigorously identify an appropriate conserved quantity in the fully kinetic Vlasov-Maxwell system, we revisit the standard “canonical helicity” construction [e.g., 71–75], in which canonical helicity is defined from the species canonical momentum and thus unifies magnetic and flow topology in a single quantity. In two-fluid/extended MHD regimes—relevant to collisionless reconnection and sub-ion dynamics—the familiar magnetic, cross [13, 110], and kinetic [6] helicity components are generally not separately invariant [111]; rather, they exchange through the model’s nonideal couplings and are redistributed by fluxes across scales and boundaries [112]. Canonical helicity evolution then ‘closes’ on these exchanges, so the apparent non-conservation of the individual components is interpreted primarily as internal conversion, plus boundary/nonideal flux terms, rather than a failure of the underlying generalized invariant [72]. Guided by this logic, we seek a fully kinetic analogue that reduces to canonical helicity in the appropriate fluid limit and that remains meaningful when fluid notions of velocity and flux-freezing become ambiguous. Accordingly, we start from the Vlasov-Maxwell system for each species

$$\partial_t f_\iota + \mathbf{v} \cdot \nabla f_\iota + \frac{q_\iota}{m_\iota} \left( \mathbf{E} + \frac{\mathbf{v}}{c} \times \mathbf{B} \right) \cdot \partial_{\mathbf{v}} f_\iota = 0, \quad (29a)$$

$$c \nabla \times \mathbf{E} = -\partial_t \mathbf{B}, \quad (29b)$$

$$c \nabla \times \mathbf{B} = \partial_t \mathbf{E} + 4\pi \sum_\iota q_\iota n_\iota \mathbf{u}_\iota, \quad (29c)$$

with  $n_\iota = \int d^3v f_\iota$  the number density and  $\mathbf{u}_\iota = n_\iota^{-1} \int d^3v \mathbf{v} f_\iota$  the bulk flow. Taking the zeroth and first moments of Eq. 29a gives

$$\partial_t n_\iota + \nabla \cdot (n_\iota \mathbf{u}_\iota) = 0, \quad (30a)$$

$$\begin{aligned} m_\iota \partial_t (n_\iota \mathbf{u}_\iota) + m_\iota \nabla \cdot (n_\iota \mathbf{u}_\iota \mathbf{u}_\iota) \\ = q_\iota n_\iota \left( \mathbf{E} + \frac{\mathbf{u}_\iota}{c} \times \mathbf{B} \right) - \nabla \cdot \mathbf{\Pi}_\iota, \end{aligned} \quad (30b)$$

which may be manipulated to read

$$\partial_t \mathbf{P}_\iota = \mathbf{u}_\iota \times \mathbf{\Omega}_\iota - \frac{c}{q_\iota} \left( \nabla \mathcal{E}_\iota + \frac{1}{n_\iota} \nabla \cdot \mathbf{\Pi}_\iota \right), \quad (31)$$

where  $\mathcal{E}_\iota \equiv \frac{1}{2} m_\iota u_\iota^2 + q_\iota \varphi$  is the sum of the kinetic and electric energies of a fluid particle of species  $\iota$ ,  $\mathbf{\Pi}_\iota \equiv m_\iota \int d^3v (\mathbf{v} - \mathbf{u}_\iota)(\mathbf{v} - \mathbf{u}_\iota) f_\iota$  is the pressure tensor, and we have defined the renormalized canonical momentum and associated canonical vorticity as, respectively,

$$\mathbf{P}_\iota \equiv \mathbf{A} + (m_\iota c/q_\iota) \mathbf{u}_\iota, \quad (32a)$$

$$\mathbf{\Omega}_\iota \equiv \nabla \times \mathbf{P}_\iota = \mathbf{B} + (m_\iota c/q_\iota) \boldsymbol{\omega}_\iota, \quad (32b)$$

with  $\boldsymbol{\omega}_\iota \equiv \nabla \times \mathbf{u}_\iota$ . Note that by starting from Eq. 29a, taking velocity moments gives the exact species continuity and momentum equations, i.e., Eqs. 30a and 30b, provided we retain the full pressure tensor as a moment of  $f_\iota$ . Curling Eq. 31 gives the canonical vorticity transport

$$\partial_t \mathbf{\Omega}_\iota = \nabla \times (\mathbf{u}_\iota \times \mathbf{\Omega}_\iota) - \frac{c}{q_\iota} \nabla \times \left( \frac{1}{n_\iota} \nabla \cdot \mathbf{\Pi}_\iota \right). \quad (33)$$

Finally, Eqs. 31 and 33 yield the local continuity equation

$$\partial_t (\mathbf{P}_\iota \cdot \mathbf{\Omega}_\iota) + \nabla \cdot \mathbf{F}_\iota = \mathbf{\mathcal{H}}_\iota \cdot \mathbf{\Omega}_\iota, \quad (34)$$

where we have defined the canonical flux,

$$\mathbf{F}_\iota \equiv \mathbf{P}_\iota \times (\mathbf{\mathcal{H}}_\iota / 2 + c \nabla \varphi), \quad (35)$$

with a momentum-balance residual from rearranging the pressure tensor term via Eqs. 30a and 30b:

$$\mathbf{\mathcal{H}}_\iota \equiv (2c/q_\iota) [\partial_t (m_\iota \mathbf{u}_\iota) - q_\iota \mathbf{E}]. \quad (36)$$

The volume integral of  $\mathbf{P}_\iota \cdot \mathbf{\Omega}_\iota$  from Eq. 34 is often referred to as the canonical helicity. For two-fluid systems, You [72] explicitly frames the “relative canonical helicity” as a gauge-invariant quantity when canonical vorticity flux crosses boundaries, and argues that while species helicities can exchange, the total relative canonical helicity is globally invariant in that idealized framework. However, in the fully kinetic Vlasov-Maxwell setting, there is generally no reason for  $\mathbf{P}_\iota \cdot \mathbf{\Omega}_\iota$  to be exactly conserved because kinetic effects bundled into  $\mathbf{\mathcal{H}}_\iota \cdot \mathbf{\Omega}_\iota$  provide sources/sinks, precisely why canonical vorticity flux conservation is conditional in the first place [73, 75].

To work around the explicit source term in Eq. 34, we introduce a source-compensated density by absorbing the time-integrated source into the field definition, yielding a conservation identity

$$\partial_t \mathcal{L}_\iota + \nabla \cdot \mathbf{F}_\iota = 0, \quad (37)$$

with the locally, source-compensated, conserved density

$$\mathcal{L}_\iota \equiv \mathbf{P}_\iota \cdot \mathbf{\Omega}_\iota - \int_{t_0}^t dt' (\mathbf{\mathcal{H}}_\iota \cdot \mathbf{\Omega}_\iota)(t'). \quad (38)$$

Equation 37 is therefore an exact conservation statement for  $\mathcal{L}_\iota$  by construction, within the continuum Vlasov-Maxwell equations. This is a mathematically legitimate step, but physically  $\mathcal{L}_\iota$  is not the usual notion of an invariant because it depends on an arbitrary reference time  $t_0$ , it is history-dependent, i.e., nonlocal in time, and it is explicitly an accounting identity rather than a topological constraint. These distinctions matter, particularly when we utilize  $\mathcal{L}_\iota$  to constrain decay scalings because the canonical helicity literature [e.g., 72, 113] treats the source terms as physical channels that genuinely create/destroy or exchange helicities, rather than something to be removed by redefinition. Nevertheless, what is important for our considerations is that Eq. 37 describes an exact conservation law that carries no two-fluid or MHD reduction and holds for fully kinetic Vlasov-Maxwell systems.

It is useful to decompose  $\mathcal{L}_\iota$  into four separate source-compensated components  $\mathcal{L}_{\iota,l}$ , with  $l = 1, 2, 3$ , and 4, that obey their own respective continuity-type equations analogous to Eq. 37,

$$\partial_t \mathcal{L}_{\iota,l} + \nabla \cdot \mathbf{F}_{\iota,l} = 0, \quad (39)$$

with

$$(\mathcal{L}_\iota, \nabla \cdot \mathbf{F}_\iota) = \sum_{l=1}^4 (\mathcal{L}_{\iota,l}, \nabla \cdot \mathbf{F}_{\iota,l}), \quad (40)$$

and it is straightforward to verify that Eq. 39 is satisfied with the scalar fields

$$\mathcal{L}_{\iota,1} \equiv \mathcal{L}_1 \equiv h + 2c \int_{t_0}^t dt' (\mathbf{E} \cdot \mathbf{B})(t'), \quad (41a)$$

$$\mathcal{L}_{\iota,2} \equiv \frac{m_\iota^2 c^2}{q_\iota^2} \left[ h_{K\iota} - 2 \int_{t_0}^t dt' (\boldsymbol{\omega}_\iota \cdot \partial_{t'} \mathbf{u}_\iota)(t') \right], \quad (41b)$$

$$\mathcal{L}_{\iota,3} \equiv \frac{2m_\iota c}{q_\iota} \left[ h_{cl} + \int_{t_0}^t dt' (\boldsymbol{\omega}_\iota \cdot c\mathbf{E} - \mathbf{B} \cdot \partial_{t'} \mathbf{u}_\iota)(t') \right], \quad (41c)$$

$$\mathcal{L}_{\iota,4} \equiv \frac{m_\iota c}{q_\iota} (\boldsymbol{\omega}_\iota \cdot \mathbf{A} - h_{cl}), \quad (41d)$$

and the flux components

$$\mathbf{F}_{\iota,1} \equiv \mathbf{F}_1 \equiv -c(\mathbf{A} \times \mathbf{E} - \varphi \mathbf{B}), \quad (42a)$$

$$\mathbf{F}_{\iota,2} \equiv \frac{m_\iota^2 c^2}{q_\iota^2} \mathbf{u}_\iota \times \partial_t \mathbf{u}_\iota, \quad (42b)$$

$$\mathbf{F}_{\iota,3} \equiv -\frac{2m_\iota c^2}{q_\iota} \mathbf{u}_\iota \times \mathbf{E}, \quad (42c)$$

$$\mathbf{F}_{\iota,4} \equiv -\frac{m_\iota c}{q_\iota} \partial_t (\mathbf{u}_\iota \times \mathbf{A}). \quad (42d)$$

Here,  $h_{K\iota} = \mathbf{u}_\iota \cdot \boldsymbol{\omega}_\iota$  and  $h_{cl} = \mathbf{u}_\iota \cdot \mathbf{B}$  are the kinetic and cross helicity densities. Note that the  $l = 1$  component of Eq. 39 matches the magnetic helicity evolution equation (Eq. 2). The first element of the source-compensated density (Eq. 41a) reduces in the ideal MHD limit to the magnetic helicity density

$$\mathcal{L}_1 \xrightarrow{\text{ideal MHD}} h, \quad (43)$$

in 2D MHD the second element (Eq. 41b) becomes the kinetic helicity density [114]

$$\frac{q_\iota^2 \mathcal{L}_{\iota,2}}{m_\iota^2 c^2} \xrightarrow{\text{2D MHD}} h_K, \quad (44)$$

and the third element (Eq. 41c) reduces in the incompressible ideal MHD limit, with mass density  $\rho = \text{const}$ , to the cross helicity density [115]

$$\frac{q_\iota \mathcal{L}_{\iota,3}}{2m_\iota c} \xrightarrow{\text{inc.-ideal MHD}} h_c. \quad (45)$$

The fourth element of the source-compensated density (Eq. 41d) informs us that  $\boldsymbol{\omega}_\iota \cdot \mathbf{A}$  is the same as cross helicity density up to a divergence.

It is worthwhile to check if  $\mathcal{L}_\iota$  and  $\mathcal{L}_{\iota,l}$  are gauge-invariant by applying the transformations  $\mathbf{A} \rightarrow \mathbf{A}' = \mathbf{A} + \nabla \chi$  and  $c\varphi \rightarrow c\varphi' = c\varphi - \partial_t \chi$ , resulting in

$$\int_V d^d x \delta_\chi \mathcal{L}_\iota = \oint_{\partial V} \chi \boldsymbol{\Omega}_\iota \cdot d\mathbf{S}, \quad (46a)$$

$$\int_V d^d x \delta_\chi \mathcal{L}_1 = \oint_{\partial V} \chi \mathbf{B} \cdot d\mathbf{S}, \quad (46b)$$

$$\int_V d^d x \delta_\chi \mathcal{L}_{\iota,2} = \int_V d^d x \delta_\chi \mathcal{L}_{\iota,3} = 0, \quad (46c)$$

$$\int_V d^d x \delta_\chi \mathcal{L}_{\iota,4} = \frac{m_\iota c}{q_\iota} \oint_{\partial V} \chi \boldsymbol{\omega}_\iota \cdot d\mathbf{S}. \quad (46d)$$

Hence  $\mathcal{L}_1$  ( $\mathcal{L}_{\iota,4}$ ) is gauge-invariant when the surface of the volume  $V$  is arranged such that it is always normal to the magnetic field (vorticity) direction, i.e.,  $\mathbf{B} \cdot \hat{\mathbf{n}} = 0$  ( $\boldsymbol{\omega}_\iota \cdot \hat{\mathbf{n}} = 0$ ) on the surface  $\partial V$ , and  $\mathcal{L}_{\iota,2}$  and  $\mathcal{L}_{\iota,3}$  are gauge-invariant without additional boundary constraints. From Eq. 46a, gauge-invariance of  $\mathcal{L}_\iota$  is sufficiently guaranteed if  $\boldsymbol{\Omega}_\iota \cdot \hat{\mathbf{n}} = 0$  on  $\partial V$ , which can be achieved if we assume that canonical vorticity structures are localized and arbitrarily small compared to  $V$  as  $V \rightarrow \infty$ . This is the analogous argument to that of Hosking and Schekochihin [26], applied in our case to the canonical vorticity instead of the magnetic field.

Equations 37 and 39 provide strictly local conservation statements for  $\mathcal{L}_\iota$  and  $\mathcal{L}_{\iota,l}$ , but in a globally nonhelical, sign-indefinite field it does not follow that the corresponding domain-integrated quantities are useful. Indeed, for an initially random configuration the full-box integrals,

$$\mathcal{L}_{V\iota} = \int_V d^d x \mathcal{L}_\iota(\mathbf{x}), \quad (47a)$$

$$\mathcal{L}_{V\iota,l} = \int_V d^d x \mathcal{L}_{\iota,l}(\mathbf{x}), \quad (47b)$$

can vanish, or remain small, by cancellation even while individual structures contain finite  $\mathcal{L}_\iota$  and  $\mathcal{L}_{\iota,l}$ . In such circumstances the appropriate global measures are instead the typical fluctuation content of the locally conserved densities on scales large compared to an interaction region but small compared to the system size. Following the logic used for nonhelical MHD decay, we therefore consider a Saffman-type correlation integral, analogous to  $\mathcal{I}_H$ ,

$$\mathcal{I}_{\mathcal{L}\iota}(R) = \int_{V_R} d^d r \langle \mathcal{L}_\iota(\mathbf{x}) \mathcal{L}_\iota(\mathbf{x} + \mathbf{r}) \rangle, \quad (48)$$

with  $L^d \ll V_R \ll V_{\text{sys}}$ , and related integrals for the conserved components of  $\mathcal{L}_\iota$ ,

$$\mathcal{I}_{\mathcal{L}\iota,l}(R) = \int_{V_R} d^d r \langle \mathcal{L}_{\iota,l}(\mathbf{x}) \mathcal{L}_{\iota,l}(\mathbf{x} + \mathbf{r}) \rangle. \quad (49)$$

Should they exist, we denote the plateau values of  $\mathcal{I}_{\mathcal{L}\iota}(R)$  and  $\mathcal{I}_{\mathcal{L}\iota,l}(R)$  as  $I_{\mathcal{L}\iota}$  and  $I_{\mathcal{L}\iota,l}$ , respectively. Under approximate homogeneity and isotropy, Eqs. 37 and 39 imply (see, e.g., Appendix B of Hosking and Schekochihin [26])

$$-\frac{1}{2} \frac{dI_{\mathcal{L}\iota}}{dt} = \int_{V_R} d^d r \nabla_{\mathbf{r}} \cdot \langle \mathcal{L}_\iota(\mathbf{x}) \mathbf{F}_\iota(\mathbf{x} + \mathbf{r}) \rangle, \quad (50a)$$

$$-\frac{1}{2} \frac{dI_{\mathcal{L}\iota,l}}{dt} = \int_{V_R} d^d r \nabla_{\mathbf{r}} \cdot \langle \mathcal{L}_{\iota,l}(\mathbf{x}) \mathbf{F}_{\iota,l}(\mathbf{x} + \mathbf{r}) \rangle, \quad (50b)$$

whose *r.h.s.* can vanish, i.e., there are intermediate-scale invariants that survive finite-box effects [27], if the  $\mathbf{r}$ -space flux terms have vanishing surface fluxes at large radii; under isotropy this is ensured by

$$\begin{aligned} \hat{\mathbf{r}} \cdot \langle \mathcal{L}_\iota(\mathbf{x}) \mathbf{F}_\iota(\mathbf{x} + \mathbf{r}) \rangle, \hat{\mathbf{r}} \cdot \langle \mathcal{L}_{\iota,l}(\mathbf{x}) \mathbf{F}_{\iota,l}(\mathbf{x} + \mathbf{r}) \rangle \\ = o(r^{1-d}), \end{aligned} \quad (51)$$

for  $L \ll r \ll L_{\text{sys}}$ .

We reason that the derivation here applies for 2D3V PIC, such as the numerical code we utilize for this work (see Appendix A) because the source-compensated densities,  $\mathcal{L}_\iota$  and  $\mathcal{L}_{\iota,l}$ , and the kinetic Saffman integral plateau values,  $I_{\mathcal{L}\iota}$  and  $I_{\mathcal{L}\iota,l}$ , remain well-defined in 2D

systems with 3D fields and velocities that are planar- (in  $x$ - $y$ ) isotropic, provided the same conditions used in 3D hold. Due to computational constraints, we exclusively consider 2D3V simulations and leave 3D3V studies for future work. In our 2D3V runs we treat these assumptions as working hypotheses and assess them empirically via the emergence of  $L \ll R \ll L_{\text{sys}}$  plateaus.

Assuming ergodicity, i.e., that spatial sampling over our periodic domain is representative of an ensemble average [e.g., 26], we may arrive at

$$I_{\mathcal{L}\iota} = \lim_{V_R \rightarrow \infty} \frac{1}{V_R} \langle \mathcal{L}_{V\iota}^2 \rangle, \quad (52a)$$

$$I_{\mathcal{L}\iota,l} = \lim_{V_R \rightarrow \infty} \frac{1}{V_R} \langle \mathcal{L}_{V\iota,l}^2 \rangle. \quad (52b)$$

Through Eqs. 52a and 52b,  $I_{\mathcal{L}\iota}$  and  $I_{\mathcal{L}\iota,l}$  are gauge-invariant under the same boundary/localization assumptions that render  $\mathcal{L}_{V\iota}$  and  $\mathcal{L}_{V\iota,l}$  meaningful.

Focusing on the electron component,  $I_{\mathcal{L}e}$ , for sub-ion dynamics, Fig. 6 shows the time evolution of  $\langle \mathcal{L}_{V\iota}^2 \rangle/V$ ,  $\langle \mathcal{L}_{V,1}^2 \rangle/V$ , and  $\langle H_V^2 \rangle/V$  [116], with  $V = L_w^2$  the window area, from our globally nonhelical simulations. This figure demonstrates that  $I_{\mathcal{L}e}$  and  $I_{\mathcal{L},1}$ , the estimated plateau values of  $\langle \mathcal{L}_{V\iota}^2 \rangle/V$  and  $\langle \mathcal{L}_{V,1}^2 \rangle/V$ , remain approximately constant over the interval and window sizes where  $L \ll R \ll L_{\text{sys}}$  [117] plateaus are identifiable, e.g., compared to the evolution of  $I_H$  depicted in both Figs. 6 and 5, the latter plotting the approximate plateau values in Fig. 6. Although Fig. 5 indicates that both  $I_{\mathcal{L}e}$  and  $I_{\mathcal{L},1}$  demonstrate near constancy,  $I_{\mathcal{L},1}$  appears slightly less invariant than  $I_{\mathcal{L}e}$  and, as shown in Fig. 6,  $\langle \mathcal{L}_{V,1}^2 \rangle/V$  seems to exhibit more variation at small scales than  $\langle \mathcal{L}_{V\iota}^2 \rangle/V$  for both mass ratios simulated.  $I_{\mathcal{L}e}$  likely appears better conserved because the additional kinetic components in  $\mathcal{L}_e = \sum_l \mathcal{L}_{e,l}$  may introduce rapidly decorrelating cross-terms that partially cancel the longer-range  $\mathcal{L}_1$  contributions in  $\hat{\mathbf{r}} \cdot \langle \mathcal{L}_e(\mathbf{x}) \mathbf{F}_e(\mathbf{x} + \mathbf{r}) \rangle$ , consistent with two-fluid/extended MHD treatments in which the canonical helicity construction is often better suited for interpreting apparent magnetic, cross, and kinetic helicity-like non-conservation as internally exchanging components [72, 73, 118].

The fact that approximately time-independent plateaus show up in these plots is consistent with  $\mathcal{L}_e$  and  $\mathcal{L}_1$  having finite effective correlation lengths over the measured interval and that subvolume boundary fluxes that would change  $\langle \mathcal{L}_{V\iota}^2 \rangle/V$  and  $\langle \mathcal{L}_{V,1}^2 \rangle/V$  are not building up system-spanning correlations, i.e., Eq. 51 is satisfied. This is the same decorrelation assumption that underpins conservation of  $I_H$  in nonhelical MHD [e.g., 26, 29], now applied to  $I_{\mathcal{L}e}$  and  $I_{\mathcal{L},1}$  in our case.

Immediately evident in Fig. 6 is that although the plateau values of  $\langle \mathcal{L}_{V\iota}^2 \rangle/V$  and  $\langle \mathcal{L}_{V,1}^2 \rangle/V$  remain approximately constant throughout both globally nonhelical simulations, the small-window component of the curves exhibit slight upward shifts during the early stages of

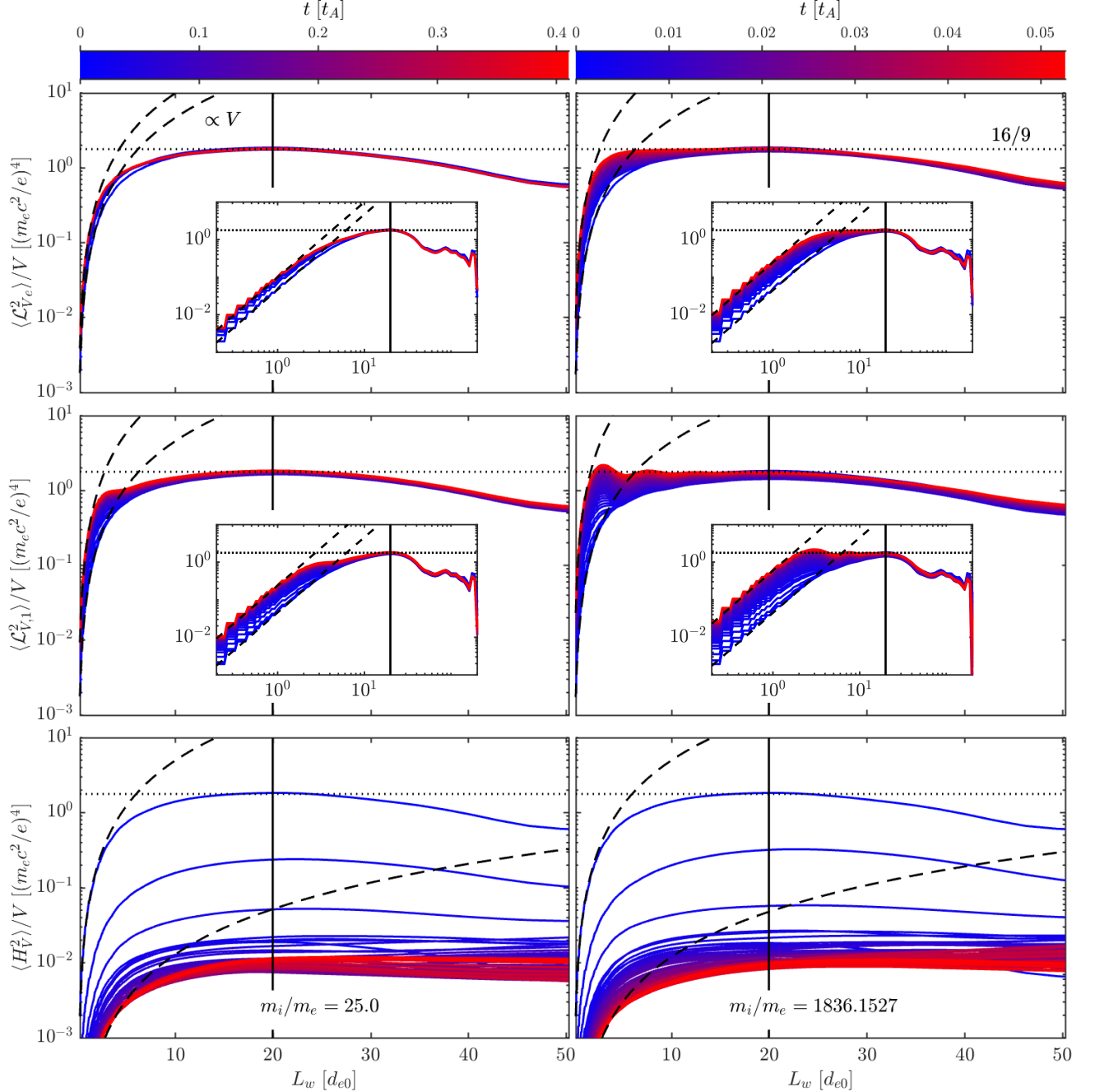


FIG. 6. Demonstration of the approximate invariance of  $I_{\mathcal{L}e}$  (upper row) and  $I_{\mathcal{L},1}$  (middle row), calculated via  $\langle \mathcal{L}_{V,e}^2 \rangle / V$  and  $\langle \mathcal{L}_{V,1}^2 \rangle / V$ , respectively, for  $m_i/m_e = 25$  (left column) and  $\approx 1836$  (right column). The lower row shows the estimator for  $I_H$  ( $\langle H_V^2 \rangle / V$ ), whose plateau values vary by over two orders of magnitude during the evolution. Included (dotted black) is the calculated value of  $I_{\mathcal{L},1}(t = 0) = I_H(t = 0)$  ( $= I_{\mathcal{L}e}(t = 0)$  for initially zero flow), derived in Appendix B, and  $\propto V = L_w^2$  curves (dashed black) for small window sizes. The solid black lines show the window size at which we calculate  $I_{\mathcal{L}e}$ ,  $I_{\mathcal{L},1}$ , and  $I_H$ , plotted in Fig. 5.

the simulation, more so for the realistic mass-ratio run. We interpret this shift as an increase in the local variance/intensity of  $\mathcal{L}_e$  and  $\mathcal{L}_1$  at small- $R$ . Because there exists a much wider separation between ion and electron

scales with  $m_i/m_e \approx 1836$  compared to the  $m_i/m_e = 25$  case, the cascade possibly has room to develop a more pronounced electron-scale range that can raise  $\langle \mathcal{L}_{V,e}^2 \rangle / V$  and  $\langle \mathcal{L}_{V,1}^2 \rangle / V$  at small  $R$  over time, even while the large-

window fluctuation content stays fixed, consistent with the behavior of a rugged constraint that governs large-scale/self-similar evolution, while small-scale physics controls intermittency and dissipation-range details [119–121].

It is worth noting that as a direct consequence of the reduction Eq. 43, the first kinetic Saffman integral (or the “magnetic integral”),  $\mathcal{I}_{\mathcal{L},1}(R)$ , in the ideal MHD limit reduces to the Hosking integral

$$\mathcal{I}_{\mathcal{L},1}(R) \underset{\text{ideal MHD}}{\rightarrow} \mathcal{I}_H(R). \quad (53)$$

To demonstrate this point, we show in Fig. 5 the time-evolution of  $I_H$ , which indicates that during late stages of the evolution, when the peak of the magnetic energy spectrum reaches scales beyond  $d_e$ , occurring at times  $t \gtrsim 0.22 t_A$  for  $m_i/m_e = 25$  and  $t \gtrsim 0.033 t_A$  for  $m_i/m_e \approx 1836$ ,  $I_H$  becomes better conserved as  $\mathbf{E} \cdot \mathbf{B}$  becomes comparatively small and the time-history contribution evolves much more slowly and/or when  $\mathbf{E} \cdot \mathbf{B}$  becomes statistically uncorrelated with structure-handedness proxies, as explored in Section II. This transition results in  $I_H$  approaching a constant offset set by the earlier kinetic stage.

From the observed invariance of the kinetic Saffman integrals, we can extract a scaling constraint by connecting the magnetic integral construction to the macroscopic similarity variables measured in our simulations. As discussed in Section II, early-time interactions occur in a regime where nonideality depletes magnetic helicity while remaining closely tied to magnetic energy conversion (see, e.g., Eq. 20). This motivated introducing  $\mathcal{L}_1$  as an event-local helicity-balance density (Eqs. 27 and 41a), which is constant in time when fluxes are negligible. We then made the working assumption—motivated by single-scale structure geometry and by the empirical association of the interaction length  $L$  with both magnetic helicity depletion and energy conversion—that the characteristic amplitude of  $\mathcal{L}_1$  in an interaction scales as  $\mathcal{L}_1 \sim B^2 L$  (Eq. 28) up to order-unity, event-dependent factors. Substituting this estimate into the Saffman integral scaling, e.g., Eq. 52b, and taking the relevant 2D3V interaction area  $V = L^2$ , we obtain

$$I_{\mathcal{L},1}^{1/4} \sim \left[ \frac{1}{V} (B^2 L)^2 V^2 \right]^{1/4} = BL \sim \text{const}, \quad (54)$$

from approximate invariance of  $I_{\mathcal{L},1}$  [122]. Equation 54 therefore provides a plausible mechanism—under approximate single-scale self-similarity—by which the  $BL \sim \text{const}$  constraint can persist in our decaying 2D3V PIC regime, even though the usual 2D MHD invariant arguments that lead to  $BL \sim \text{const}$  do not directly apply. For example, in 2D MHD turbulence, the scaling  $BL \sim \text{const}$  follows directly from writing Eq. 4. In the ideal limit the mean-square out-of-plane magnetic vector potential  $\int d^2x |A_z|^2$ , sometimes termed anastrophy, is a rugged invariant [19, 123–128], and since dimensionally  $A_{z,\text{rms}} \sim BL$ , approximate conservation of  $\int d^2x |A_z|^2$

implies  $BL \sim \text{const}$  [26]. In fully kinetic 2D3V systems, however,  $\int d^2x |A_z|^2$  is generally not conserved because phase-space cascades, Landau damping, and finite-Larmor-radius effects introduce additional channels [129]. Here we have presented a fully kinetic argument for the constancy of  $BL$  in 2D3V without appealing to frozen-in flux or to 2D MHD anastrophy conservation.

Applying the integral scale definition [e.g., 27]

$$L \equiv \frac{\int_0^\infty dk k^{-1} \mathcal{E}_B(k)}{\int_0^\infty dk \mathcal{E}_B(k)}, \quad (55)$$

we show numerical evidence in agreement with the  $BL \sim \text{const}$  scaling in Fig. 7, which plots both  $BL$  and  $B^2 L$ , with the latter monotonically decreasing on average, for both initially net-helical and nonhelical simulations. Although the arguments presented in this section may provide an explanation as to why we find that  $BL \sim \text{const}$  for our initially nonhelical runs, it is interesting that Fig. 7 should also show this to be the case in our initially net-helical simulations. We explore this point of contention in the following section.

We return now to the interpretation of our 2D3V simulation results that like-helicity interactions predominantly reduce structures’ magnetic helicity while leaving the interaction-scale magnetic amplitude combination  $B_s^2 L_s$  only weakly altered over the event (e.g., Eq. 28), with  $B_s$  and  $L_s$  the structure-level magnetic field amplitude and size measures. To parameterize the helical content of a structure  $s$ , we introduce a structure fractional helicity  $\sigma_s \equiv h_s/(B_s^2 L_s)$ , where  $h_s$  denotes the characteristic magnetic helicity density in  $V_s$ , i.e.,  $h_s \sim H_{V_s}/V_s$ .

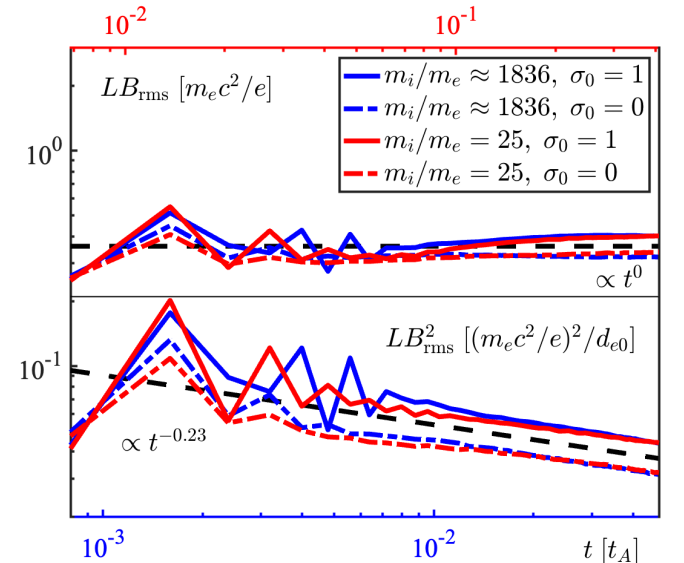


FIG. 7. Numerical verification of  $BL \sim \text{const}$  (Eq. 54) over all 2D3V PIC simulations (upper panel). The evolution of  $B^2 L$  (lower panel) is included for reference. The black dashed lines plot the power-law scalings:  $\propto t^0$  in the upper panel and  $\propto t^{-0.23}$  in the lower panel, determined from a linear least-squares fit of the  $m_i/m_e \approx 1836$  and  $\sigma_0 = 0$  run.

With this definition, combined with Eq. 20, changes in  $|h_s|$  decompose as

$$\frac{d|h_s|}{dt} = B_s^2 L_s \frac{d}{dt} |\sigma_s| + |\sigma_s| \frac{d}{dt} (B_s^2 L_s) \sim L_s \frac{d}{dt} (B_s^2). \quad (56)$$

Recall that in Section II, for globally nonhelical fields during the early kinetic stage, we found that  $I_H \propto B^4$  (see, e.g., Fig. 5) and in this section we demonstrated numerical evidence that  $BL \sim \text{const}$  globally (e.g., Fig. 7). Assuming that at any given time  $|\sigma_s|$  and  $B_s$  are representative of the magnitude of the helical content in all magnetic structures and the global rms  $B$ , respectively, i.e., the system is approximately single-scale, we may write the approximate scaling of the Hosking integral as

$$I_H \sim h^2 V \sim |\sigma_s|^2 B^4 L^4 \sim |\sigma_s|^2 \propto B^4, \quad (57)$$

and therefore, upon utilizing Eq. 56,

$$(B_s^2 L_s)^{-1} \frac{d}{dt} (B_s^2 L_s) \sim |\sigma_s|^{-1} (|\sigma_s|^{-1} - 1) \frac{d}{dt} |\sigma_s|. \quad (58)$$

Hence when  $|\sigma_s| \sim 1$ , i.e., individual structures are near maximally helical, Eq. 58 gives

$$B_s^2 L_s \sim \text{const}, \quad (59)$$

which is compatible with our assumption from  $\mathcal{L}_1$ -conservation that like-helicity interactions are approximately  $B_s^2 L_s$ -preserving while  $|\sigma_s|$  decreases. We interpret this tendency in Eqs. 56 and 59 that the dominant contribution to the decline of  $|h_s|$  is a reduction of  $|\sigma_s|$ , while the residual evolution of  $B_s^2 L_s$  is subleading when  $|\sigma_s| \sim 1$  throughout the event. At later times, when  $|\sigma_s| \ll 1$ ,  $|h_s|$  and  $|\sigma_s|$  become approximately constant and these interactions again satisfy Eq. 59. For cancellation-dominated, i.e., globally nonhelical, configurations, we return to the kinetic Hosking/Saffman-style scaling derived above (Eq. 54) to obtain the global similarity constraint  $BL \sim \text{const}$  from the approximate invariance of  $I_{\mathcal{L},1}$ .

#### IV. INITIALLY NET-HELICAL FIELD

Let us now consider an initially net-helical configuration as a useful contrasting case for the scaling arguments leading to the  $BL \sim \text{const}$  constraint. Since  $\mathcal{L}_1$  provides a conserved diagnostic and scales as  $\sim B^2 L$  up to order-unity, event-dependent factors, under a straightforward extension of the MHD intuition, one might be tempted to expect that with a net-helical initial configuration, the decay should obey the scaling  $B^2 L \sim \text{const}$ , e.g., the same scaling as in MHD for net-helical fields [16, 24, 25]. In our numerical simulations with globally helical initial conditions, however, we find that although the configurations start with  $\sigma_0 = 1$ , the fields rapidly tend toward effectively nonhelical global states, i.e.,  $\sigma \rightarrow 0$ .

This trend is illustrated in Fig. 8, which shows, for our initially fully helical fields, the evolution of the windowed magnetic helicity variance  $\langle H_V^2 \rangle / V$  that, at early times, exhibits an approximately  $\propto V$  scaling across window sizes, consistent with magnetic helicity being predominantly single-signed over the accessible scales [26]. As the evolution proceeds,  $\langle H_V^2 \rangle / V$  develops a plateau over a growing range of window sizes, indicative of increasing cancellation among positive/negative contributions within those windows, and a weak residual imbalance appears to remain primarily at the largest windows.

The emergence of mixed-handed substructures is consistent with the sub-ion nonideality mechanism discussed in Section II. In our simulations,  $\mathbf{E} \cdot \mathbf{B} \neq 0$  is intermittent and localized, so different regions experience different histories of the integrated nonideal term  $-2c \int_{t_0}^t dt' \mathbf{E} \cdot \mathbf{B}$ . In regions where this term becomes comparable to or exceeds the local pre-existing helical content, the local magnetic helicity density can be driven through zero and acquire the opposite sign. Consistent with Section II, we find that  $\text{sgn}(\mathbf{E} \cdot \mathbf{B})$  predominantly agrees with  $\text{sgn}(\mathbf{E}' \cdot \mathbf{J} / \alpha)$  across the cases examined, as demonstrated in Fig. 1, so the same correlation between nonideality and structure handedness is observed within the same empirical scatter in the initially net-helical runs as well.

Since the global fractional helicity rapidly becomes increasingly cancellation-dominated, the data are most consistent with the nonhelical scaling  $BL \sim \text{const}$  over the sub-ion interval we measure, as reported by Fig. 7. At early times there is a brief transient in which the  $BL$  curve is slightly elevated relative to the  $\sigma_0 = 0$  case, consistent with an intermediate regime while the field transitions from single-signed to cancellation-dominated magnetic helicity. This transient may then contribute to slightly larger final  $LB_{\text{rms}}$  and  $LB_{\text{rms}}^2$  compared to the initially nonhelical runs, as indicated in Fig. 7.

#### V. CONCLUSIONS

Magnetic helicity has long served as a powerful organizing principle for magnetically dominated turbulence in the ideal MHD limit, where it is approximately conserved up to boundary fluxes and weak resistive effects and therefore constrains large-scale evolution and inverse transfer. Many space and astrophysical plasmas, however, transition into regimes where ion and electron dynamics decouple, current sheets thin to kinetic scales, and collisionless reconnection becomes an essential part of the cascade and dissipation. A central result of this work is that, in the class of sub-ion decaying turbulence studied here, helicity-based reasoning can be retained if reformulated in a fully kinetic manner that explicitly accounts for localized nonideality.

Directly from magnetic helicity balance, the volume term proportional to  $\int_V dV \mathbf{E} \cdot \mathbf{B}$  provides a channel for magnetic helicity change whenever parallel electric fields appear, as is commonly observed and expected in colli-

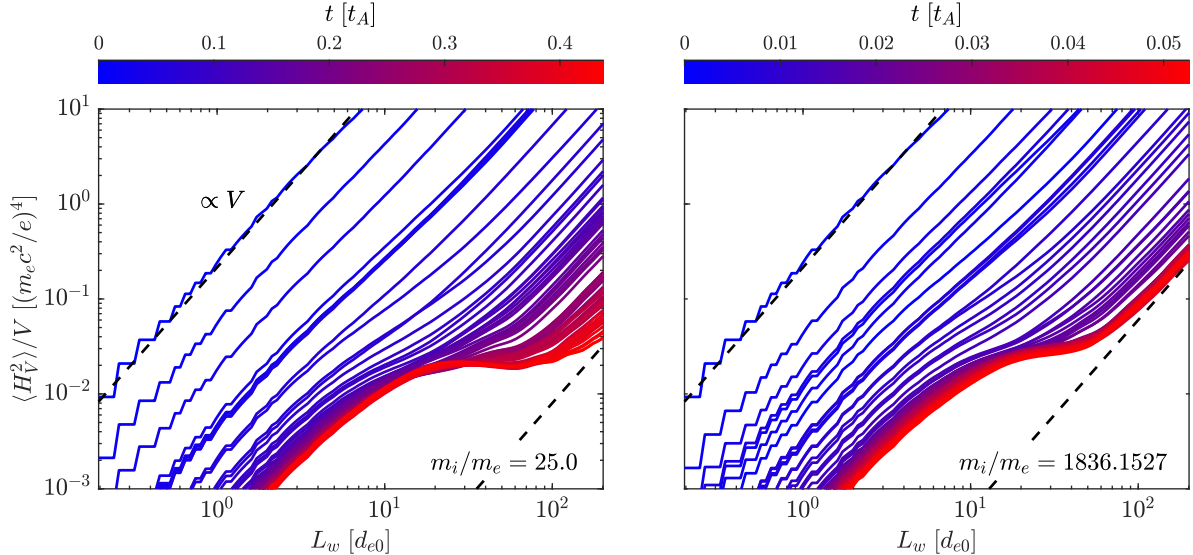


FIG. 8. Demonstration of the tendency towards zero global fractional helicity for initially net-helical configurations in both  $m_i/m_e = 25$  (left panel) and  $\approx 1836$  (right panel) runs. Included (dashed black) are  $\propto V = L_w^2$  lines at small and large window sizes, showing the behavior of  $\langle H_V^2 \rangle/V$  within individual magnetic structures and the small global helicity imbalance over larger windows.

sionless diffusion regions. In our 2D3V PIC simulations,  $\mathbf{E} \cdot \mathbf{B} \neq 0$  is intermittent and spatially localized, and, during the early kinetic stage, shows a statistically significant association with structure handedness, diagnosed via fixed-gauge magnetic and current helicity proxies, indicative of reconnection-mediated interactions that preferentially reduce the magnitude of magnetic helicity contained within individual coherent structures.

Motivated by the observed role of time-integrated  $\mathbf{E} \cdot \mathbf{B}$ , we revisited canonical vorticity transport starting from the Vlasov-Maxwell system and derived an exact local continuity equation with a kinetic source term. By absorbing the time-integrated source into a redefined, history-dependent density, we obtained a source-free conservation identity by construction and Saffman-type correlation integrals, which, under standard flux-decorrelation assumptions, can admit intermediate-scale plateaus that are time-independent. The source-compensated quantity is an exact reformulation by construction; the physically relevant question is whether intermediate-scale plateaus emerge empirically under localization assumptions. Once an approximately conserved plateau exists, it can play an analogous role as the Hosking/Saffman magnetic helicity integral plays in MHD decay theory. In the globally nonhelical case, the first kinetic Saffman integral constrains the coupled evolution of magnetic field amplitude and outer-scale under approximate single-scale self-similarity. In our 2D3V setting, invariance of the kinetic integral is consistent with the familiar nonhelical scaling  $BL \sim \text{const}$ , and our simulations show behavior compatible with this scaling over the measured sub-ion interval. Within this framework,

reconnection enters explicitly through the time-history term, so one can formulate decay constraints that remain informative across the kinetic interval when a plateau is observed.

In our simulations, initially net-helical configurations quickly develop mixed-signed magnetic helicity patches and the global fractional helicity decreases toward small values. This behavior is consistent with, and plausibly driven by, the intermittency of  $\mathbf{E} \cdot \mathbf{B}$ , where different regions accumulate different histories of the nonideal term, so local magnetic helicity density can be driven through zero and change sign. The emergence of strong sign-mixing is qualitatively consistent with the modern observational and numerical picture of kinetic turbulence as an intermittent ensemble of reconnecting structures, in which reconnection and dissipation signatures cluster around current sheets. One implication is that the presence of a net-helical bias in the initial spectrum does not automatically enforce the MHD-like  $B^2 L \sim \text{const}$  scaling over the kinetic interval examined in our 2D3V runs. Instead, kinetic reconnection can rapidly reduce the net magnetic helicity before an MHD-scale helicity constraint becomes relevant.

Observationally, turbulence in the solar wind and magnetosheath spans MHD to kinetic scales and exhibits abundant reconnection signatures and intermittent dissipation. A plausible and testable speculation is that sub-ion reconnection may often reduce the net magnetic helicity available to be inherited by larger, more MHD-like scales unless magnetic helicity is continuously injected at larger scales or through boundaries. An added potential implication concerns primordial and cosmic magnetic

fields, where helicity-based decay arguments are widely used to connect early-time magnetogenesis scenarios to present-day amplitudes and coherence lengths via inverse transfer and approximate invariants [21–23, 25, 130]. Our results suggest a caveat that if, at any stage of cosmic evolution, a substantial portion of the magnetic spectrum resides in regimes where localized kinetic/non-MHD non-ideality, including regimes where  $\mathbf{E} \cdot \mathbf{B} \neq 0$ , is dynamically important—whether due to extreme scale separation or intermittent reconnection in thin structures—then the effective fractional helicity inherited by larger, more MHD-like scales may be reduced by rapid sign-mixing. In that case, predictions that rely on near-perfect magnetic helicity conservation across all active scales can, in principle, overestimate the persistence of a net-helical bias and the strength of helical inverse transfer. This may motivate targeted tests in 3D kinetic and hybrid-kinetic settings designed to quantify when kinetic reconnection acts as an effective sign-mixing mechanism versus when net magnetic helicity survives to constrain large-scale cosmic evolution, with possible downstream consequences for inferred present-day field coherence.

We further speculate that these results may have broader implications for mean-field dynamo theory and in particular to “catastrophic  $\alpha$ -quenching,” where nonlinear saturation is constrained by the accumulation and transport of small-scale magnetic helicity and the associated current helicity contribution to the magnetic part of the turbulent mean electromotive force [131–137]. Mitigating catastrophic  $\alpha$ -quenching has motivated extensive work on helicity fluxes and other helicity-removal pathways [138–148]. Our results suggest a candidate kinetic-scale mechanism by which collisionless nonideality can reduce the helical content of localized magnetic structures, potentially acting as an effective small-scale “helicity sink” in weakly collisional plasmas where Ohmic dissipation is subdominant. We emphasize that this connection to  $\alpha$ -quenching is necessarily speculative in our 2D3V, freely decaying setting, and would require that helicity transfer couples the mean-field-relevant scales to kinetic scales in 3D.

The most valuable next steps are those that probe robustness, universality, and measurability. The existence of an intermediate-scale plateau—and the localization assumptions needed for conservation—should be tested in fully 3D kinetic turbulence. Extending the framework from freely decaying to forced turbulence would clarify whether the conserved integral constrains statistically steady-state cascades, e.g., by setting relationships between injection, intermittency, and outer-scale evolution, in the presence of sustained reconnection. Systematic scans in  $\beta$ , guide-field strength, imbalance, and scale separation can determine when the tendency toward mixed-signed magnetic helicity patches is fast across a broad range of parameters, versus when net magnetic helicity can survive the kinetic range.

## ACKNOWLEDGMENTS

The author extends his deepest gratitude to the late Nuno F. Loureiro for insightful discussions, for his immense support during the early stages of this work, and for suggesting the appropriate symbol to represent the local kinetic density  $\mathcal{L}_t$ . The author also acknowledges the OSIRIS Consortium, comprising UCLA and Instituto Superior Técnico (IST) in Lisbon, Portugal, for providing access to the OSIRIS 4.0 framework.

## FUNDING

This research was partially funded by DOE award DE-FG02-91ER54109 and utilized resources of the National Energy Research Scientific Computing Center, a DOE Office of Science User Facility, supported by the U.S. Department of Energy under Contract No. DE-AC02-05CH11231 using NERSC award FES-ERCAP0026577. This material is based upon work supported by the National Science Foundation Graduate Research Fellowship Program under Grant No. 2141064. Any opinions, findings, and conclusions or recommendations expressed in this material are those of the author and do not necessarily reflect the views of the National Science Foundation.

## Appendix A: Simulation setup

The simulations reported in this work are conducted using the PIC code OSIRIS [149, 150]. The global Alfvén time is defined as  $t_A = L_x/v_{A,0}$ , where  $v_{A,0} = B_{\text{rms},0}/(4\pi m_i n_0)^{1/2}$  is the ion Alfvén speed,  $B_{\text{rms},0} \equiv B_{\text{rms}}(t=0)$ , and  $L_x$  and  $L_y$  are the lengths of the simulation box in the  $x$  and  $y$  directions, respectively, and are equivalent. The initial ion and electron temperatures  $T_{i0}$  and  $T_{e0}$  are equal and uniform, we set  $\beta_{\text{rms}} \equiv 8\pi n_0(T_{i0} + T_{e0})/B_{\text{rms},0}^2 = 1$ , and species’ bulk flows are initialized as zero. The relationship between the electron plasma and cyclotron frequencies is given by  $\omega_{pe} = 2\Omega_{ce,\text{rms}}$  where  $\omega_{pe} = (4\pi n_0 e^2/m_e)^{1/2}$  and  $\Omega_{ce,\text{rms}} = |e|B_{\text{rms},0}/(m_e c)$ . We utilize quadratic particle interpolations and resolve the electron Debye length,  $\lambda_{De} = u_{\text{th},e}/\omega_{pe}$ , to mitigate numerical heating. Key simulation parameters used in these runs are listed in Table I.

Our magnetic field initialization is similar to that of Hosking and Schekochihin [26], but the practical implementation differs. Because OSIRIS specifies initial conditions via real-space expressions, we initialize  $\mathbf{B}$  as a finite trigonometric sum, limiting the number of modes without compromising the robustness of parsing and evaluation.

Mode amplitudes are weighted by a prescribed shape

Parameter	Value
$\lambda_{De}/d_{e0} = u_{th,e}/c$	1/4
$L_x/d_{e0} = L_y/d_{e0}$	$64\pi$
$\omega_{pe}/\Omega_{ce,\text{rms}}$	2
$T_{i0}/T_{e0}$	1
$m_i/m_e$	25.0; 1836.1527
$k_c d_{e0}$	0.5
$\beta_{\text{rms}}$	1
$M$	15
$\sigma_0$	0; 1
$a$	7
$\Delta x/\lambda_{De} = \Delta y/\lambda_{De}$	0.393
Time step ( $\omega_{pe}\Delta t$ )	0.0687
Particles-per-cell (per species)	4096 ( $64^2$ )
Resolution	$2048^2$

TABLE I. Summary of 2D3V simulation parameters.

function

$$F_0(k) \equiv F(k; t = 0) = Ak^{(a-d+1)/2} \times \exp(1 - k^2/k_c^2), \quad (\text{A1})$$

where  $a$  is a tunable parameter used to place the excited band in  $k$ -space and  $k_c$  sets its characteristic scale. Because only a narrow band of  $k$  is populated with a finite number of modes and the field is subsequently renormalized to a prescribed  $B_{\text{rms},0}$ ,  $a$  should be viewed as a parameter controlling the initial excitation scale rather than as an independently realized inertial-range exponent.

To obtain an approximately isotropic realization, we write discrete wave-vectors  $\mathbf{k}_m = (2\pi m_x/L_x, 2\pi m_y/L_y)$  and choose  $M = 15$  distinct lattice pairs  $(m_x, m_y)$ , where  $m_x, m_y \in \mathbb{Z}$ , excluding the zero mode  $(0, 0)$ . For sparse-mode initialization we center the populated ring near the wavenumber  $|\mathbf{k}| \simeq k_c$  that maximizes the quadratic magnetic weight  $k^{d-1} F_0^2(k)$ , which controls random-phase estimates of large-scale fluctuations of quadratic magnetic quantities, e.g.,  $B^2$  and Maxwell stress. For Eq. A1 this occurs at  $k_p = \sqrt{a/4k_c}$  [151].

We set the weights

$$w_{\pm}[\sigma_k(k)] = [1 \pm \sigma_k(k)]/2, \quad (\text{A2})$$

draw independent phases  $\phi_{\pm} \in \text{Unif}[0, 2\pi)$ , and set the Fourier representation of the magnetic field as

$$\mathbf{B}_k = \sqrt{F_0(k)} [\sqrt{w_+(\sigma_0)} e^{i\phi_+} \hat{\mathbf{e}}_+ + \sqrt{w_-(\sigma_0)} e^{i\phi_-} \hat{\mathbf{e}}_-], \quad (\text{A3})$$

with the helical (circular) basis

$$\hat{\mathbf{e}}_{\pm} = (\hat{\mathbf{e}}_1 \pm i\hat{\mathbf{e}}_2)/\sqrt{2}, \quad (\text{A4})$$

such that  $\hat{\mathbf{e}}_1 \perp \hat{\mathbf{k}}_m$  and  $\hat{\mathbf{e}}_2 = \hat{\mathbf{k}}_m \times \hat{\mathbf{e}}_1$ , i.e., each mode is divergence-free and  $(\hat{\mathbf{e}}_1, \hat{\mathbf{e}}_2, \hat{\mathbf{k}}_m)$  is right-handed. For each mode, the real-space contribution of  $B_{j,\mathbf{k}_m}$  is

$$B_{j,m}(\mathbf{x}) = \Re\{B_{j,\mathbf{k}_m} e^{i\mathbf{k}_m \cdot \mathbf{x}}\} = \alpha_{j,m} \cos(\mathbf{k}_m \cdot \mathbf{x}) - \beta_{j,m} \sin(\mathbf{k}_m \cdot \mathbf{x}), \quad (\text{A5})$$

where  $\alpha_{j,m} = \Re\{B_{j,\mathbf{k}_m}\}$  and  $\beta_{j,m} = \Im\{B_{j,\mathbf{k}_m}\}$ . Finally, we write

$$B_j(x, y) = \sum_{m=1}^M A_{j,m} \cos(k_{xm}x + k_{ym}y + \phi_{j,m}), \quad (\text{A6})$$

with

$$A_{j,m} = \sqrt{\alpha_{j,m}^2 + \beta_{j,m}^2}, \quad (\text{A7a})$$

$$\phi_{j,m} = \text{atan2}(\beta_{j,m}, \alpha_{j,m}). \quad (\text{A7b})$$

Over a periodic box, the spatial average of  $|\mathbf{B}|^2$  is

$$\langle |\mathbf{B}|^2 \rangle_{V_{\text{sys}}} = \frac{1}{V_{\text{sys}}} \int d^2x |\mathbf{B}|^2 = \sum_{m=1}^M \sum_{j=1}^3 \frac{A_{j,m}^2}{2}. \quad (\text{A8})$$

Thus all coefficients are rescaled by  $\sqrt{2}B_{\text{rms},0}/(\sum_{m=1}^M \sum_{j=1}^3 A_{j,m}^2)^{1/2}$ .

## Appendix B: Evaluation of the numerical value of the first kinetic Saffman integral

A useful aspect of the first kinetic Saffman integral (or the “magnetic integral”)  $\mathcal{I}_{\mathcal{L},1}(R)$  (see, e.g., Eq. 49) is that, at the reference time  $t = t_0$  used to define the history term,  $\mathcal{L}_1(t_0) = h(t_0)$  (e.g., Eq. 41a), also equivalent to  $\mathcal{L}_t(t_0)$  for initially zero bulk flows, and therefore the corresponding plateau values of the correlation integrals coincide:

$$I_{\mathcal{L},1}(t_0) = I_H(t_0) \quad (\text{B1})$$

and  $\simeq I_{\mathcal{L}_t}(t_0)$  for magnetically dominated systems. Under homogeneity/ergodicity and scale separation,  $I_H$  corresponds to the  $L \ll R \ll L_{\text{sys}}$  plateau of the volume-averaged magnetic helicity variance. A convenient Fourier characterization is that, for statistically isotropic fields, the isotropized helicity-variance spectrum [26, 27],

$$\Theta(k) = \frac{S_{d-1} k^{d-1}}{(2\pi)^d} \int d^d r \langle h(\mathbf{x})h(\mathbf{x} + \mathbf{r}) \rangle e^{-i\mathbf{k} \cdot \mathbf{r}}, \quad (\text{B2})$$

obeys

$$\Theta(k \rightarrow 0) = \frac{S_{d-1}}{(2\pi)^d} I_H k^{d-1} + o(k^{d-1}), \quad (\text{B3})$$

and therefore

$$I_H = \lim_{k \rightarrow 0} \frac{(2\pi)^d}{S_{d-1}} k^{-(d-1)} \Theta(k). \quad (\text{B4})$$

Let us now assume, in the isotropic continuum approximation, a random-phase construction (Appendix A)

in which the helical weights are allowed to be scale-dependent:

$$\mathbf{B}_k = \sqrt{F(k)} \{ \sqrt{w_+[\sigma_k(k)]} e^{i\phi_+} \hat{\mathbf{e}}_+ + \sqrt{w_-[\sigma_k(k)]} e^{i\phi_-} \hat{\mathbf{e}}_- \}, \quad (\text{B5})$$

where  $F(k)$  sets the spectrum of the magnetic field via Eq. 23.

Here  $\mathbf{B}_k$  is the complex synthesis amplitude used in Appendix A, i.e., the coefficient that appears inside a real-field contribution  $\Re\{\mathbf{B}_k e^{i\mathbf{k}\cdot\mathbf{x}}\}$ . Expanding the real part,

$$\Re\{\mathbf{B}_k e^{i\mathbf{k}\cdot\mathbf{x}}\} = \frac{1}{2} \mathbf{B}_k e^{i\mathbf{k}\cdot\mathbf{x}} + \frac{1}{2} \mathbf{B}_k^* e^{-i\mathbf{k}\cdot\mathbf{x}}, \quad (\text{B6})$$

so a single synthesis term contributes Fourier series coefficients  $\mathcal{B}_k = \mathbf{B}_k/2$  and  $\mathcal{B}_{-\mathbf{k}} = \mathbf{B}_k^*/2$ , and likewise  $\mathcal{A}_k = \mathbf{A}_k/2$ . If both  $\pm\mathbf{k}$  appear in the discrete synthesis set, then the net Fourier series coefficient at  $\mathbf{k}$  is  $\mathcal{B}_k = (\mathbf{B}_k + \mathbf{B}_{-\mathbf{k}}^*)/2$  and similarly for  $\mathcal{A}_k$ . For the isotropic continuum estimate below we adopt the standard convention in which one representative per  $\pm\mathbf{k}$  pair is used; with that convention the factors 1/4 in Eq. B16 and 1/16 in Eq. B14 follow directly from the 1/2 factors above. With the Fourier transform convention  $\tilde{\mathbf{B}}(\mathbf{k}) = \int_V d^d x \mathbf{B}(\mathbf{x}) e^{-i\mathbf{k}\cdot\mathbf{x}}$ , one has  $\tilde{\mathbf{B}}(\mathbf{k}) = V^{1/2} \mathcal{B}_k$  and similarly for  $\tilde{\mathbf{A}}(\mathbf{k})$ .

For each Fourier mode in Coulomb-gauge,

$$i\mathbf{k} \times \hat{\mathbf{e}}_{\pm} = \pm k \hat{\mathbf{e}}_{\pm}, \quad (\text{B7})$$

and thus Eq. B5 implies

$$\mathbf{A}_k = \frac{\sqrt{F(k)}}{k} \{ \sqrt{w_+[\sigma_k(k)]} e^{i\phi_+} \hat{\mathbf{e}}_+ - \sqrt{w_-[\sigma_k(k)]} e^{i\phi_-} \hat{\mathbf{e}}_- \}. \quad (\text{B8})$$

The Fourier transform of  $h$  is the convolution

$$\tilde{h}(\mathbf{k}) = \frac{V}{4} \int \frac{d^d k'}{(2\pi)^d} \mathbf{A}_{k'} \cdot \mathbf{B}_{\mathbf{k}-\mathbf{k'}}. \quad (\text{B9})$$

To connect to  $\Theta(k)$ , we consider, with Eq. B9,

$$\langle |\tilde{h}(\mathbf{k})|^2 \rangle = \frac{V^2}{16} \int \frac{d^d k'}{(2\pi)^d} \int \frac{d^d k''}{(2\pi)^d} \langle (\mathbf{A}_{k'} \cdot \mathbf{B}_{\mathbf{k}-\mathbf{k'}}) \times (\mathbf{A}_{k''} \cdot \mathbf{B}_{\mathbf{k}-\mathbf{k''}})^* \rangle. \quad (\text{B10})$$

With random phases, the phase average eliminates most cross terms. However, there are two distinct phase-matching contraction channels that survive in Eq. B10: (i) the direct contraction  $\mathbf{k}'' = \mathbf{k}'$ , and (ii) the exchange contraction  $\mathbf{k}'' = \mathbf{k} - \mathbf{k}'$ . In the limit  $\mathbf{k} \rightarrow 0$ , these become  $\mathbf{k}'' = \mathbf{k}'$  and  $\mathbf{k}'' \simeq -\mathbf{k}'$ , respectively, and under isotropy and  $\mathbf{k} \leftrightarrow -\mathbf{k}$  symmetry the two contributions are equal. Therefore, Eq. B10 gives

$$\lim_{k \rightarrow 0} \frac{1}{V} \langle |\tilde{h}(\mathbf{k})|^2 \rangle = \frac{1}{8} \int \frac{d^d k'}{(2\pi)^d} \langle |\mathbf{A}_{k'} \cdot \mathbf{B}_{-\mathbf{k}'}|^2 \rangle. \quad (\text{B11})$$

A straightforward average over the independent phases  $\phi_{\pm}$  yields, from Eqs. B5 and B8,

$$\begin{aligned} \langle |\mathbf{A}_{k'} \cdot \mathbf{B}_{-\mathbf{k}'}|^2 \rangle &= 2w_+w_- \frac{F^2(k')}{k'^2} \\ &= \frac{1 - \sigma_k^2(k')}{2} \frac{F^2(k')}{k'^2}. \end{aligned} \quad (\text{B12})$$

Substituting Eq. B12 into Eq. B11 gives

$$\begin{aligned} \lim_{k \rightarrow 0} \frac{1}{V} \langle |\tilde{h}(\mathbf{k})|^2 \rangle &= \frac{1}{16} \int \frac{d^d k'}{(2\pi)^d} [1 - \sigma_k^2(k')] \\ &\quad \times \frac{F^2(k')}{k'^2}. \end{aligned} \quad (\text{B13})$$

Combining Eq. B13 with the small- $k$  form of  $\Theta(k)$  above (equivalently, Zhou *et al.* [27]'s Eqs. 2.14 and 2.15) yields

$$I_H \simeq \frac{1}{16} \frac{S_{d-1}}{(2\pi)^d} \int_0^\infty dk [1 - \sigma_k^2(k)] k^{d-3} F^2(k), \quad (\text{B14})$$

which was referenced as Eq. 22 in Section II. With our specific  $F(k; t = 0) = F_0(k)$  (Eq. A1) and if  $\sigma_k(k; t = 0) \simeq \sigma_0$  over the contributing scales, Eq. B14 becomes

$$\begin{aligned} I_H(t = 0) &\simeq (1 - \sigma_0^2) \frac{S_{d-1}}{(2\pi)^d} A^2 e^2 k_c^{a-1} \\ &\quad \times 2^{-(a+9)/2} \Gamma\left(\frac{a-1}{2}\right). \end{aligned} \quad (\text{B15})$$

With  $\langle |\mathbf{B}|^2 \rangle_{V_{\text{sys}}} = B_{\text{rms}}^2$ , then, with our convention  $|\mathbf{B}_k|^2 = F(k)$ ,

$$\begin{aligned} B_{\text{rms},0}^2 &= \frac{1}{4} \frac{S_{d-1}}{(2\pi)^d} \int_0^\infty dk k^{d-1} F_0(k) = \frac{1}{8} \frac{S_{d-1}}{(2\pi)^d} \\ &\quad \times A e k_c^{(a+d+1)/2} \Gamma\left(\frac{a+d+1}{4}\right). \end{aligned} \quad (\text{B16})$$

Substituting Eq. B16 into Eq. B15 yields

$$\begin{aligned} I_H(t = 0) &\simeq (1 - \sigma_0^2) \frac{(2\pi)^d}{S_{d-1}} B_{\text{rms},0}^4 k_c^{-(d+2)} \\ &\quad \times 2^{-(a-3)/2} \frac{\Gamma(\frac{a-1}{2})}{\Gamma^2(\frac{a+d+1}{4})}. \end{aligned} \quad (\text{B17})$$

Equation B17 gives, in the isotropic continuum approximation, for  $a = 7$ ,  $d = 2$ ,  $\sigma_0 = 0$ ,  $B_{\text{rms},0} [m_e c^2 / (ed_{e0})] = 0.5$ , and  $k_c [d_{e0}^{-1}] = 0.5$  (see, e.g., Table I),  $I_H(t = 0) [(m_e c^2/e)^4] = 16/9$ , which we use as a reference value for comparison in Figs. 5 and 6 as the black dotted lines. For the finite- $M$  thin-ring initialization used in the simulations, Eq. B17 should be interpreted as an isotropic-continuum reference estimate. The corresponding discrete expression is obtained by replacing the continuum integrals with sums over the discrete Fourier series coefficients  $\mathcal{B}_k$  and  $\mathcal{A}_k$  associated with the initialized real field, with  $\mathcal{B}_k$  receiving contributions from any synthesized  $\pm\mathbf{k}$  terms as described above. Access to the  $k \rightarrow 0$  regime additionally requires a domain large enough to support Fourier modes well below the populated ring.

[1] W. M. Elsasser, *Reviews of Modern Physics* **28**, 135–163 (1956).

[2] L. Woltjer, *Proceedings of the National Academy of Sciences* **44**, 489–491 (1958).

[3] M. A. Berger and G. B. Field, *Journal of Fluid Mechanics* **147**, 133–148 (1984).

[4] A. H. Boozer, *The Physics of Fluids* **29**, 4123–4130 (1986).

[5] V. I. Arnold and B. A. Khesin, *Topological Methods in Hydrodynamics* (Springer International Publishing, 2021).

[6] H. K. Moffatt, *Journal of Fluid Mechanics* **35**, 117–129 (1969).

[7] H. K. Moffatt and R. L. Ricca, *Proceedings of the Royal Society of London. Series A: Mathematical and Physical Sciences* **439**, 411–429 (1992).

[8] J. B. Taylor, *Physical Review Letters* **33**, 1139–1141 (1974).

[9] J. B. Taylor, *Reviews of Modern Physics* **58**, 741–763 (1986).

[10] H. Ji, S. C. Prager, and J. S. Sarff, *Physical Review Letters* **74**, 2945–2948 (1995).

[11] H. Y. Guo, A. L. Hoffman, K. E. Miller, and L. C. Steinhauer, *Physical Review Letters* **92**, 10.1103/physrevlett.92.245001 (2004).

[12] E. G. Blackman, Magnetic helicity and large scale magnetic fields: A primer, in *Multi-scale Structure Formation and Dynamics in Cosmic Plasmas* (Springer New York, 2016) p. 59–91.

[13] U. Frisch, A. Pouquet, J. LÉOrat, and A. Mazure, *Journal of Fluid Mechanics* **68**, 769–778 (1975).

[14] D. Biskamp and W.-C. Müller, *Physical Review Letters* **83**, 2195–2198 (1999).

[15] W.-C. Müller and D. Biskamp, *Physical Review Letters* **84**, 475–478 (2000).

[16] M. Christensson, M. Hindmarsh, and A. Brandenburg, *Physical Review E* **64**, 10.1103/physreve.64.056405 (2001).

[17] A. Alexakis, P. D. Mininni, and A. Pouquet, *The Astrophysical Journal* **640**, 335–343 (2006).

[18] A. Pouquet, D. Rosenberg, J. Stawarz, and R. Marino, *Earth and Space Science* **6**, 351–369 (2019).

[19] W. H. Matthaeus and D. Montgomery, *Annals of the New York Academy of Sciences* **357**, 203–222 (1980).

[20] T. Stribling, W. H. Matthaeus, and S. Oughton, *Physics of Plasmas* **2**, 1437–1452 (1995).

[21] R. Banerjee and K. Jedamzik, *Physical Review D* **70**, 10.1103/physrevd.70.123003 (2004).

[22] R. Durrer and A. Neronov, *The Astronomy and Astrophysics Review* **21**, 10.1007/s00159-013-0062-7 (2013).

[23] K. Subramanian, *Reports on Progress in Physics* **79**, 076901 (2016).

[24] G. B. Field and S. M. Carroll, *Physical Review D* **62**, 10.1103/physrevd.62.103008 (2000).

[25] C. Caprini and L. Sorbo, *Journal of Cosmology and Astroparticle Physics* **2014** (10), 056–056.

[26] D. N. Hosking and A. A. Schekochihin, *Physical Review X* **11**, 10.1103/physrevx.11.041005 (2021).

[27] H. Zhou, R. Sharma, and A. Brandenburg, *Journal of Plasma Physics* **88**, 10.1017/s002237782200109x (2022).

[28] A. Brandenburg and A. Banerjee, *Journal of Plasma Physics* **91**, 10.1017/s0022377824001508 (2025).

[29] J. K. J. Hew, D. N. Hosking, C. Federrath, J. R. Beattie, and N. Kriel, *Conservation of magnetic-helicity fluctuations due to spatial decorrelation of fluxes in decaying mhd turbulence* (2025).

[30] A. Brandenburg and G. Larsson, *Atmosphere* **14**, 932 (2023).

[31] A. Armua, A. Berera, and J. Calderón-Figueroa, *Physical Review E* **107**, 10.1103/physreve.107.055206 (2023).

[32] D. N. Hosking and A. A. Schekochihin, *Nature Communications* **14**, 10.1038/s41467-023-43258-3 (2023).

[33] M. Yamada, R. Kulsrud, and H. Ji, *Reviews of Modern Physics* **82**, 603–664 (2010).

[34] R. Bruno and V. Carbone, *Living Reviews in Solar Physics* **10**, 10.12942/lrsp-2013-2 (2013).

[35] O. Alexandrova, C. H. K. Chen, L. Sorriso-Valvo, T. S. Horbury, and S. D. Bale, *Space Science Reviews* **178**, 101–139 (2013).

[36] D. Verscharen, K. G. Klein, and B. A. Maruca, *Living Reviews in Solar Physics* **16**, 10.1007/s41116-019-0021-0 (2019).

[37] F. Sahraoui, L. Hadid, and S. Huang, *Reviews of Modern Plasma Physics* **4**, 10.1007/s41614-020-0040-2 (2020).

[38] J. M. Finn and T. M. Antonsen, Jr, Magnetic helicity: what is it and what is it good for (1985).

[39] K. Schindler, M. Hesse, and J. Birn, *Journal of Geophysical Research: Space Physics* **93**, 5547–5557 (1988).

[40] E. G. Zweibel and M. Yamada, *Annual Review of Astronomy and Astrophysics* **47**, 291–332 (2009).

[41] M. A. Shay, J. F. Drake, B. N. Rogers, and R. E. Denton, *Geophysical Research Letters* **26**, 2163–2166 (1999).

[42] M. A. Shay, J. F. Drake, B. N. Rogers, and R. E. Denton, *Journal of Geophysical Research: Space Physics* **106**, 3759–3772 (2001).

[43] J. Drake and M. Shay, *Reconnection of Magnetic Fields*. Cambridge University Press, New York, NY , 87 (2007).

[44] D. Tsiklauri and T. Haruki, *Physics of Plasmas* **15**, 10.1063/1.2999532 (2008).

[45] R. A. Treumann and W. Baumjohann, *Frontiers in Physics* **1**, 10.3389/fphy.2013.00031 (2013).

[46] L. Comisso and A. Bhattacharjee, *Journal of Plasma Physics* **82**, 10.1017/s002237781600101x (2016).

[47] P. A. Cassak, Y.-H. Liu, and M. A. Shay, *Journal of Plasma Physics* **83**, 10.1017/s0022377817000666 (2017).

[48] M. Wan, W. H. Matthaeus, H. Karimabadi, V. Roytershteyn, M. Shay, P. Wu, W. Daughton, B. Loring, and S. C. Chapman, *Physical Review Letters* **109**, 10.1103/physrevlett.109.195001 (2012).

[49] M. Wan, W. H. Matthaeus, V. Roytershteyn, H. Karimabadi, T. Parashar, P. Wu, and M. Shay, *Physical Review Letters* **114**, 10.1103/physrevlett.114.175002 (2015).

[50] J. M. TenBarge and G. G. Howes, *The Astrophysical Journal* **771**, L27 (2013).

[51] C. C. Haggerty, T. N. Parashar, W. H. Matthaeus, M. A. Shay, Y. Yang, M. Wan, P. Wu, and S. Servidio, *Physics of Plasmas* **24**, 10.1063/1.5001722 (2017).

[52] S. Servidio, F. Valentini, F. Califano, and P. Veltri, *Physical Review Letters* **108**, 10.1103/phys-

revlett.108.045001 (2012).

[53] S. Servidio, K. T. Osman, F. Valentini, D. Perrone, F. Califano, S. Chapman, W. H. Matthaeus, and P. Veltri, *The Astrophysical Journal* **781**, L27 (2014).

[54] L. Franci, S. Landi, L. Matteini, A. Verdini, and P. Hellinger, *The Astrophysical Journal* **812**, 21 (2015).

[55] L. Franci, S. Landi, A. Verdini, L. Matteini, and P. Hellinger, *The Astrophysical Journal* **853**, 26 (2018).

[56] L. Sorriso-Valvo, D. Perrone, O. Pezzi, F. Valentini, S. Servidio, I. Zouganelis, and P. Veltri, *Journal of Plasma Physics* **84**, 10.1017/s0022377818000302 (2018).

[57] K. T. Osman, W. H. Matthaeus, M. Wan, and A. F. Rappazzo, *Physical Review Letters* **108**, 10.1103/physrevlett.108.261102 (2012).

[58] K. T. Osman, W. H. Matthaeus, J. T. Gosling, A. Greco, S. Servidio, B. Hnat, S. C. Chapman, and T. D. Phan, *Physical Review Letters* **112**, 10.1103/physrevlett.112.215002 (2014).

[59] A. Chasapis, A. Retinò, F. Sahraoui, A. Vaivads, Y. V. Khotyaintsev, D. Sundkvist, A. Greco, L. Sorriso-Valvo, and P. Canu, *The Astrophysical Journal* **804**, L1 (2015).

[60] A. Chasapis, Y. Yang, W. H. Matthaeus, T. N. Parashar, C. C. Haggerty, J. L. Burch, T. E. Moore, C. J. Pollock, J. Dorelli, D. J. Gershman, R. B. Torbert, and C. T. Russell, *The Astrophysical Journal* **862**, 32 (2018).

[61] Z. Vörös, E. Yordanova, A. Varsani, K. J. Genestreti, Y. V. Khotyaintsev, W. Li, D. B. Graham, C. Norgren, R. Nakamura, Y. Narita, F. Plaschke, W. Magnes, W. Baumjohann, D. Fischer, A. Vaivads, E. Eriksson, P. Lindqvist, G. Marklund, R. E. Ergun, M. Leitner, M. P. Leubner, R. J. Strangeway, O. Le Contel, C. Pollock, B. J. Giles, R. B. Torbert, J. L. Burch, L. A. Avanov, J. C. Dorelli, D. J. Gershman, W. R. Paterson, B. Lavraud, and Y. Saito, *Journal of Geophysical Research: Space Physics* **122**, 10.1002/2017ja024535 (2017).

[62] R. Bandyopadhyay, W. H. Matthaeus, T. N. Parashar, Y. Yang, A. Chasapis, B. L. Giles, D. J. Gershman, C. J. Pollock, C. T. Russell, R. J. Strangeway, R. B. Torbert, T. E. Moore, and J. L. Burch, *Physical Review Letters* **124**, 10.1103/physrevlett.124.255101 (2020).

[63] E. Yordanova, Z. Vörös, A. Varsani, D. B. Graham, C. Norgren, Y. V. Khotyaintsev, A. Vaivads, E. Eriksson, R. Nakamura, P. Lindqvist, G. Marklund, R. E. Ergun, W. Magnes, W. Baumjohann, D. Fischer, F. Plaschke, Y. Narita, C. T. Russell, R. J. Strangeway, O. Le Contel, C. Pollock, R. B. Torbert, B. J. Giles, J. L. Burch, L. A. Avanov, J. C. Dorelli, D. J. Gershman, W. R. Paterson, B. Lavraud, and Y. Saito, *Geophysical Research Letters* **43**, 5969–5978 (2016).

[64] T. D. Phan, J. P. Eastwood, M. A. Shay, J. F. Drake, B. U. O. Sonnerup, M. Fujimoto, P. A. Cassak, M. Øieroset, J. L. Burch, R. B. Torbert, A. C. Rager, J. C. Dorelli, D. J. Gershman, C. Pollock, P. S. Pyakurel, C. C. Haggerty, Y. Khotyaintsev, B. Lavraud, Y. Saito, M. Oka, R. E. Ergun, A. Retino, O. Le Contel, M. R. Argall, B. L. Giles, T. E. Moore, F. D. Wilder, R. J. Strangeway, C. T. Russell, P. A. Lindqvist, and W. Magnes, *Nature* **557**, 202–206 (2018).

[65] J. E. Stawarz, J. P. Eastwood, T. D. Phan, I. L. Gingell, M. A. Shay, J. L. Burch, R. E. Ergun, B. L. Giles, D. J. Gershman, O. L. Contel, P.-A. Lindqvist, C. T. Russell, R. J. Strangeway, R. B. Torbert, M. R. Argall, D. Fischer, W. Magnes, and L. Franci, *The Astrophysical Journal Letters* **877**, L37 (2019).

[66] P. Sharma Pyakurel, M. A. Shay, T. D. Phan, W. H. Matthaeus, J. F. Drake, J. M. TenBarge, C. C. Haggerty, K. G. Klein, P. A. Cassak, T. N. Parashar, M. Swisdak, and A. Chasapis, *Physics of Plasmas* **26**, 10.1063/1.5090403 (2019).

[67] C. Vega, V. Roytershteyn, G. L. Delzanno, and S. Boldyrev, *The Astrophysical Journal Letters* **893**, L10 (2020).

[68] A. Mallet, *Journal of Plasma Physics* **86**, 10.1017/s0022377819000941 (2020).

[69] F. Califano, S. S. Cerri, M. Faganello, D. Laveder, M. Sisti, and M. W. Kunz, *Frontiers in Physics* **8**, 10.3389/fphy.2020.00317 (2020).

[70] Z. Liu, C. Silva, L. M. Milanese, M. Zhou, N. R. Mandell, and N. F. Loureiro, *Physical Review Letters* **134**, 10.1103/physrevlett.134.155201 (2025).

[71] L. C. Steinhauer, H. Yamada, and A. Ishida, *Physics of Plasmas* **8**, 4053–4061 (2001).

[72] S. You, *Physics of Plasmas* **19**, 10.1063/1.4752215 (2012).

[73] S. You, *Physics of Plasmas* **23**, 10.1063/1.4956465 (2016).

[74] Y. D. Yoon and P. M. Bellan, *Physics of Plasmas* **24**, 10.1063/1.4982812 (2017).

[75] Y. D. Yoon, *AAPPs Bulletin* **35**, 10.1007/s43673-025-00146-w (2025).

[76] W. H. Matthaeus, M. L. Goldstein, and C. Smith, *Physical Review Letters* **48**, 1256–1259 (1982).

[77] W. H. Matthaeus and M. L. Goldstein, *Journal of Geophysical Research: Space Physics* **87**, 6011–6028 (1982).

[78] G. G. Howes and E. Quataert, *The Astrophysical Journal* **709**, L49–L52 (2010).

[79] H. R. Strauss, *The Physics of Fluids* **19**, 134–140 (1976).

[80] At each output time we reconstruct the full magnetic vector potential  $\mathbf{A}(x, y) = (A_x, A_y, A_z)$  from  $\mathbf{B}(x, y)$  on the doubly periodic domain by spectral inversion of the Poisson problem  $\nabla^2 \mathbf{A} = -\nabla \times \mathbf{B}$ , equivalently  $\tilde{\mathbf{A}}(\mathbf{k}) = i\mathbf{k} \times \tilde{\mathbf{B}}(\mathbf{k})/|\mathbf{k}|^2$  for  $\mathbf{k} \neq 0$ , with the mean mode fixed by  $\tilde{\mathbf{A}}(\mathbf{0}) = \mathbf{0}$ . This yields the periodic Coulomb-gauge representative,  $\nabla \cdot \mathbf{A} = 0$ , and removes the residual constant-offset freedom.

[81] N. Seehafer, *Solar Physics* **125**, 219–232 (1990).

[82] M. Hagino and T. Sakurai, *Publications of the Astronomical Society of Japan* **56**, 831–843 (2004).

[83] A. A. Pevtsov, M. A. Berger, A. Nindos, A. A. Norton, and L. van Driel-Gesztelyi, *Space Science Reviews* **186**, 285–324 (2014).

[84] T. Wiegelmann and T. Sakurai, *Living Reviews in Solar Physics* **9**, 10.12942/lrsp-2012-5 (2012).

[85] S. Zenitani, M. Hesse, A. Klimas, and M. Kuznetsova, *Physical Review Letters* **106**, 10.1103/physrevlett.106.195003 (2011).

[86] S. Zenitani, M. Hesse, A. Klimas, C. Black, and M. Kuznetsova, *Physics of Plasmas* **18**, 10.1063/1.3662430 (2011).

[87] S. Zenitani, I. Shinohara, and T. Nagai, *Geophysical Research Letters* **39**, 10.1029/2012gl051938 (2012).

[88] J. L. Burch, R. B. Torbert, T. D. Phan, L.-J. Chen, T. E. Moore, R. E. Ergun, J. P. Eastwood, D. J. Gershman, P. A. Cassak, M. R. Argall, S. Wang, M. Hesse, C. J. Pollock, B. L. Giles, R. Nakamura, B. H. Mauk,

S. A. Fuselier, C. T. Russell, R. J. Strangeway, J. F. Drake, M. A. Shay, Y. V. Khotyaintsev, P.-A. Lindqvist, G. Marklund, F. D. Wilder, D. T. Young, K. Torkar, J. Goldstein, J. C. Dorelli, L. A. Avanov, M. Oka, D. N. Baker, A. N. Jaynes, K. A. Goodrich, I. J. Cohen, D. L. Turner, J. F. Fennell, J. B. Blake, J. Clemmons, M. Goldman, D. Newman, S. M. Petrinec, K. J. Trattner, B. Lavraud, P. H. Reiff, W. Baumjohann, W. Magnes, M. Steller, W. Lewis, Y. Saito, V. Coffey, and M. Chandler, *Science* **352**, 10.1126/science.aaf2939 (2016).

[89] R. B. Torbert, J. L. Burch, T. D. Phan, M. Hesse, M. R. Argall, J. Shuster, R. E. Ergun, L. Alm, R. Nakamura, K. J. Genestreti, D. J. Gershman, W. R. Paterson, D. L. Turner, I. Cohen, B. L. Giles, C. J. Pollock, S. Wang, L.-J. Chen, J. E. Stawarz, J. P. Eastwood, K. J. Hwang, C. Farrugia, I. Dors, H. Vaith, C. Mouikis, A. Ardakani, B. H. Mauk, S. A. Fuselier, C. T. Russell, R. J. Strangeway, T. E. Moore, J. F. Drake, M. A. Shay, Y. V. Khotyaintsev, P.-A. Lindqvist, W. Baumjohann, F. D. Wilder, N. Ahmadi, J. C. Dorelli, L. A. Avanov, M. Oka, D. N. Baker, J. F. Fennell, J. B. Blake, A. N. Jaynes, O. Le Contel, S. M. Petrinec, B. Lavraud, and Y. Saito, *Science* **362**, 1391–1395 (2018).

[90] K. J. Genestreti, R. Nakamura, Y.-H. Liu, J. L. Burch, C. Norgren, J. Shuster, M. Hesse, R. B. Torbert, L.-J. Chen, and S. V. Heuer, *Space Science Reviews* **221**, 10.1007/s11214-025-01188-0 (2025).

[91] M. Yamada, J. Yoo, J. Jara-Almonte, H. Ji, R. M. Kulsrud, and C. E. Myers, *Nature Communications* **5**, 10.1038/ncomms5774 (2014).

[92] V. Wilder, R. E. Ergun, J. L. Burch, N. Ahmadi, S. Eriksson, T. D. Phan, K. A. Goodrich, J. Shuster, A. C. Rager, R. B. Torbert, B. L. Giles, R. J. Strangeway, F. Plaschke, W. Magnes, P. A. Lindqvist, and Y. V. Khotyaintsev, *Journal of Geophysical Research: Space Physics* **123**, 6533–6547 (2018).

[93] W. Fox, V. Wilder, S. Eriksson, J. Jara-Almonte, F. Pucci, J. Yoo, H. Ji, M. Yamada, R. E. Ergun, M. Øieroset, and T. D. Phan, *Geophysical Research Letters* **45**, 10.1029/2018gl079883 (2018).

[94] J. T. Dahlin, J. F. Drake, and M. Swisdak, *Physics of Plasmas* **21**, 10.1063/1.4894484 (2014).

[95] J. T. Dahlin, J. F. Drake, and M. Swisdak, *Physics of Plasmas* **23**, 10.1063/1.4972082 (2016).

[96] S. Eriksson, F. D. Wilder, R. E. Ergun, S. J. Schwartz, P. A. Cassak, J. L. Burch, L.-J. Chen, R. B. Torbert, T. D. Phan, B. Lavraud, K. A. Goodrich, J. C. Holmes, J. E. Stawarz, A. P. Sturner, D. M. Malaspina, M. E. Usanova, K. J. Trattner, R. J. Strangeway, C. T. Russell, C. J. Pollock, B. L. Giles, M. Hesse, P.-A. Lindqvist, J. F. Drake, M. A. Shay, R. Nakamura, and G. T. Marklund, *Physical Review Letters* **117**, 10.1103/physrevlett.117.015001 (2016).

[97] J. P. Eastwood, R. Mistry, T. D. Phan, S. J. Schwartz, R. E. Ergun, J. F. Drake, M. Øieroset, J. E. Stawarz, M. V. Goldman, C. Haggerty, M. A. Shay, J. L. Burch, D. J. Gershman, B. L. Giles, P. A. Lindqvist, R. B. Torbert, R. J. Strangeway, and C. T. Russell, *Geophysical Research Letters* **45**, 4569–4577 (2018).

[98] J. H. Poynting, *Philosophical Transactions of the Royal Society of London*, 343–361 (1884).

[99] S. E. Gralla and T. Jacobson, *Monthly Notices of the Royal Astronomical Society* **445**, 2500–2534 (2014).

[100] S. E. Gralla and N. Iqbal, *Physical Review D* **99**, 10.1103/physrevd.99.105004 (2019).

[101] Y. Narita, *Nonlinear Processes in Geophysics* **24**, 203–214 (2017).

[102] A. Brandenburg, *The Astrophysical Journal* **550**, 824–840 (2001).

[103] In our PIC simulations  $\mathbf{u}_i$  and  $\mathbf{u}_e$  are outputted as proper velocities, i.e.,  $\mathbf{u} = \gamma \mathbf{v}$ , with  $\gamma = (1 - v^2/c^2)^{-1/2}$  the Lorentz factor. Since the flows we observe in our numerical experiments are only mildly relativistic, with  $\gamma \simeq 1$  over the domains of interest, replacing  $\mathbf{v}$  with the proper velocity in the moment-based current introduces only  $\mathcal{O}(\gamma - 1)$  corrections and does not significantly affect the sign-based helicity-alignment diagnostics.

[104] The interval over which  $I_H$  becomes approximately stationary may also be associated with times in which  $\mathbf{E} \cdot \mathbf{B}$  becomes comparatively small as the dominant scales move above electron kinetic scales, as discussed in Section III.

[105] S. Banerjee and S. Galtier, *Physical Review E* **93**, 10.1103/physreve.93.033120 (2016).

[106] A. Alexakis and L. Biferale, *Physics Reports* **767–769**, 1–101 (2018).

[107] D. Grošelj, C. H. K. Chen, A. Mallet, R. Samtaney, K. Schneider, and F. Jenko, *Physical Review X* **9**, 10.1103/physrevx.9.031037 (2019).

[108] J. Squire, R. Meyrand, M. W. Kunz, L. Arzamasskiy, A. A. Schekochihin, and E. Quataert, *Nature Astronomy* **6**, 715–723 (2022).

[109] J. E. Stawarz, P. A. Muñoz, N. Bessho, R. Bandyopadhyay, T. K. M. Nakamura, S. Eriksson, D. B. Graham, J. Büchner, A. Chasapis, J. F. Drake, M. A. Shay, R. E. Ergun, H. Hasegawa, Y. V. Khotyaintsev, M. Swisdak, and F. D. Wilder, *Space Science Reviews* **220**, 10.1007/s11214-024-01124-8 (2024).

[110] L. Woltjer, *Proceedings of the National Academy of Sciences* **44**, 833–841 (1958).

[111] M. Lingam, P. J. Morrison, and G. Miloshevich, *Physics of Plasmas* **22**, 10.1063/1.4926821 (2015).

[112] A. Pouquet and N. Yokoi, *Philosophical Transactions of the Royal Society A: Mathematical, Physical and Engineering Sciences* **380**, 10.1098/rsta.2021.0087 (2022).

[113] A. Brandenburg, Importance of magnetic helicity in dynamos, in *Cosmic Magnetic Fields* (Springer Berlin Heidelberg, 2005) p. 219–253.

[114] For 2D MHD,  $\mathbf{u} = \hat{\mathbf{z}} \times \nabla \phi \rightarrow \partial_t \mathbf{u} = \hat{\mathbf{z}} \times \nabla(\partial_t \phi)$  and  $\boldsymbol{\omega} = \nabla \times \mathbf{u} = \hat{\mathbf{z}} \nabla^2 \phi$ , with  $\phi$  the stream function. Thus,  $\boldsymbol{\omega} \cdot \partial_t \mathbf{u} = 0$ .

[115] In incompressible ideal MHD, with the mass density  $\rho = \text{const}$ , the integrand of Eq. 41c may be written as, with  $p$  the scalar pressure,  $\boldsymbol{\omega} \cdot c\mathbf{E} - \mathbf{B} \cdot \partial_t \mathbf{u} = \nabla \cdot [(u^2/2 + p/\rho)\mathbf{B}]$ , which is a pure divergence and can thus be completely absorbed into  $\mathbf{F}_{4,3}$ .

[116] We compute  $\langle \mathcal{L}_{V_e}^2 \rangle/V$ ,  $\langle \mathcal{L}_{V,1}^2 \rangle/V$ , and  $\langle H_V^2 \rangle/V$  from gridded 2D snapshots of  $\mathcal{L}_e$ ,  $\mathcal{L}_1$ , and  $h$  by sliding a rectangular window over all positions with periodic wraparound, summing the scalar fields within each window to form window-integral maps, or equivalently, circular convolutions with rectangular top-hat kernels. We then average the squared window integrals and normalize by the window area. For mean-zero stationary fields, this quantity is an area-weighted measure of the fields' two-point correlation within the chosen window scale.

[117] Note that the decrease in  $\langle \mathcal{L}_{V_e}^2 \rangle / V$  and  $\langle \mathcal{L}_{V,1}^2 \rangle / V$  at large  $L_w$  in each panel of Fig. 6 are finite-size artifacts, as the full-box integral is exactly zero by construction.

[118] J. von der Linden, J. Sears, T. Intrator, and S. You, *Physical Review Letters* **121**, 10.1103/physrevlett.121.035001 (2018).

[119] A. N. Kolmogorov, *Proceedings of the Royal Society of London. Series A: Mathematical and Physical Sciences* **434**, 9–13 (1991).

[120] P. Goldreich and S. Sridhar, *The Astrophysical Journal* **438**, 763 (1995).

[121] U. Frisch, *Turbulence: The Legacy of A.N. Kolmogorov* (Cambridge University Press, 1995).

[122] The scaling in Eq. 54 is also consistent with random-walk arguments for structure coalescence in the absence of a nonzero mean helicity [e.g., 26].

[123] D. Fyfe and D. Montgomery, *Journal of Plasma Physics* **16**, 181–191 (1976).

[124] D. Fyfe, D. Montgomery, and G. Joyce, *Journal of Plasma Physics* **17**, 369–398 (1977).

[125] T. Hatori, *Journal of the Physical Society of Japan* **53**, 2539–2545 (1984).

[126] A. C. Ting, W. H. Matthaeus, and D. Montgomery, *The Physics of Fluids* **29**, 3261–3274 (1986).

[127] D. Biskamp and H. Welter, *Physics of Fluids B: Plasma Physics* **1**, 1964–1979 (1989).

[128] D. Biskamp and E. Schwarz, *Physics of Plasmas* **8**, 3282–3292 (2001).

[129] In 2D3V, the out-of-plane magnetic vector potential  $A_z$  evolves as  $\partial_t A_z = -cE_z$  and hence the evolution equation for anastrophy  $\mathcal{A} \equiv \int d^2x |A_z|^2$  includes a source term  $-c \int d^2x A_z E_z$ . We find in the numerical experiments presented in this work that  $\mathcal{A}$  is generally not conserved, even during late stages of the system evolution (not shown in this paper).

[130] D. Grasso and H. R. Rubinstein, *Physics Reports* **348**, 163–266 (2001).

[131] A. Pouquet, U. Frisch, and J. Léorat, *Journal of Fluid Mechanics* **77**, 321–354 (1976).

[132] A. V. Gruzinov and P. H. Diamond, *Physical Review Letters* **72**, 1651–1653 (1994).

[133] F. Cattaneo and D. W. Hughes, *Physical Review E* **54**, R4532–R4535 (1996).

[134] E. T. Vishniac and J. Cho, *The Astrophysical Journal* **550**, 752–760 (2001).

[135] G. B. Field and E. G. Blackman, *The Astrophysical Journal* **572**, 685–692 (2002).

[136] E. G. Blackman and G. B. Field, *Physical Review Letters* **89**, 10.1103/physrevlett.89.265007 (2002).

[137] A. Brandenburg and K. Subramanian, *Physics Reports* **417**, 1–209 (2005).

[138] S. I. Vainshtein and F. Cattaneo, *The Astrophysical Journal* **393**, 165 (1992).

[139] E. G. Blackman and G. B. Field, *The Astrophysical Journal* **534**, 984–988 (2000).

[140] A. Brandenburg, A. Bigazzi, and K. Subramanian, *Monthly Notices of the Royal Astronomical Society* **325**, 685–692 (2001).

[141] A. Brandenburg and W. Dobler, *Astronomy & Astrophysics* **369**, 329–338 (2001).

[142] A. Brandenburg and C. Sandin, *Astronomy & Astrophysics* **427**, 13–21 (2004).

[143] A. Brandenburg, S. Candelaresi, and P. Chatterjee, *Monthly Notices of the Royal Astronomical Society* **398**, 1414–1422 (2009).

[144] N. Kleeorin, D. Moss, I. Rogachevskii, and D. Sokoloff, *Astronomy & Astrophysics* **387**, 453–462 (2002).

[145] K. Subramanian and A. Brandenburg, *Physical Review Letters* **93**, 10.1103/physrevlett.93.205001 (2004).

[146] S. Sur, A. Shukurov, and K. Subramanian, *Monthly Notices of the Royal Astronomical Society* **377**, 874–882 (2007).

[147] D. Mitra, D. Moss, R. Tavakol, and A. Brandenburg, *Astronomy & Astrophysics* **526**, A138 (2011).

[148] F. Del Sordo, G. Guerrero, and A. Brandenburg, *Monthly Notices of the Royal Astronomical Society* **429**, 1686–1694 (2012).

[149] R. A. Fonseca *et al.*, *Proceedings of The International Conference on Computer Science* **2331**, 342 (2002).

[150] R. G. Hemker, arXiv:1503.00276. [Online]. Available: <http://arxiv.org/abs/1503.00276> (2015).

[151] The helicity-variance integral that defines  $I_H$  carries an additional factor  $k^{-2}$  (e.g., Eq. 22), shifting the dominant band to  $|\mathbf{k}| = \sqrt{(a-2)/4k_c}$ ; This differs from  $k_p$  only by  $\approx 15\%$  for  $a = 7$  used here. For  $d = 2$ ,  $k_p$  differs from  $\sqrt{(a+d-1)/4k_c}$ , the peak of the initial shell-integrated magnetic energy spectrum  $\propto k^{d-1} F_0(k)$ , by  $\approx 7\%$  and from the reciprocal of the initial “effective magnetic helicity density correlation length,”  $L_h^{-1}(t = 0)$ , (i.e., Eq. 25) by  $\approx 4\%$ .